



Optical properties and simple forcing efficiency of the organic aerosols and black carbon emitted by residential wood burning in rural Central Europe

5 Andrea Cuesta-Mosquera¹, Kristina Glojek², Griša Močnik^{2,3,4}, Luka Drinovec^{2,3,4}, Asta Gregorič^{2,5},
Martin Rigler⁵, Matej Ogrin⁶, Baseerat Romshoo¹, Kay Weinhold¹, Maik Merkel¹, Dominik van
Pinxteren⁷, Hartmut Herrmann⁷, Alfred Wiedensohler¹, Mira Pöhlker¹, Thomas Müller¹

¹Department of Experimental Aerosol and Cloud Microphysics, Leibniz Institute for Tropospheric Research (TROPOS), Leipzig, 04318, Germany

²Center for Atmospheric Research, University of Nova Gorica, Ajdovščina, 5270, Slovenia

10 ³Department of Condensed Matter Physics, Jožef Stefan Institute, Ljubljana, 1000, Slovenia

⁴Haze Instruments d.o.o., Ljubljana, 1000, Slovenia

⁵Aerosol d.o.o., Ljubljana, 1000, Slovenia

⁶Department of Geography, Faculty of Arts, University of Ljubljana, Ljubljana, 1000, Slovenia

⁷Atmospheric Chemistry Department, Leibniz Institute for Tropospheric Research (TROPOS), Leipzig, 04318, Germany

15 *Correspondence to:* Andrea Cuesta-Mosquera (cuesta@tropos.de, andrea.cuesta2305@gmail.com)

Abstract. Recent years have seen an increase in the use of wood for energy production of over 30%, and this trend is expected to continue due to the current energy crisis and geopolitical instability. At present, residential wood burning (RWB) is one of the most important sources of organic aerosols (OA) and black carbon (BC). While BC is recognized for its large light absorption cross-section, the role of OA in light absorption is still under evaluation due to their heterogeneous composition and source-dependent optical properties. Studies that characterize wood-burning aerosol emissions in Europe typically focus on urban and background sites and only cover BC properties. However, RWB is more prevalent in rural areas, and the present scenario indicates that an improved understanding of the RWB aerosol optical properties and their subsequent connection to climate impacts is necessary for rural areas.

25 We have characterized atmospheric aerosol particles from a central European rural site during wintertime in the village of Retje in Loški Potok, Slovenia, from 01.12.2017 to 07.03.2018. The village experienced extremely high aerosol concentrations produced by RWB and near-ground temperature inversion. The isolated location of the site and the substantial local emissions made it an ideal laboratory-like place for characterizing RWB aerosols with low influence from non-RWB sources under ambient conditions. The mean mass concentrations of OA and BC were $34.8 \mu\text{g m}^{-3}$ (max = $271.8 \mu\text{g m}^{-3}$) and $3.1 \mu\text{g m}^{-3}$ (max = $24.3 \mu\text{g m}^{-3}$), respectively. The mean total particle number concentration (10–600 nm) was $9.9 \times 10^3 \text{ particles cm}^{-3}$ (max = $53.5 \times 10^3 \text{ particles cm}^{-3}$). The mean total light absorption coefficient at 370 nm and 880 nm measured by an Aethalometer AE33 were 122.8 Mm^{-1} and 15.3 Mm^{-1} and had maximum values of 1103.9 Mm^{-1} and 179.1 Mm^{-1} , respectively. The aerosol concentrations and absorption coefficients measured during the campaign in Loški Potok were significantly larger than those reported values for several urban areas in the region with larger populations and extent of aerosol sources.

Here, considerable contributions from brown carbon (BrC) to the total light absorption were identified, reaching up to 60% and 48% in the near UV (370 nm) and blue (470 nm) wavelengths. These contributions are up to three times higher than values reported for other sites impacted by wood-burning emissions. The calculated mass absorption cross-section and the absorption Ångström exponent for RWB OA were $MAC_{OA, 370\text{ nm}} = 2.4\text{ m}^2\text{ g}^{-1}$, and $AAE_{BrC, 370-590\text{ nm}} = 3.9$, respectively.

Simple forcing efficiency (SFE) calculations were performed as a sensitivity analysis to evaluate the climate impact of the RWB aerosols produced at the study site by integrating the optical properties measured during the campaign. The SFE results show a considerable forcing capacity from the local RWB aerosols, with a high sensitivity to OA absorption properties and a more substantial impact over bright surfaces like snow, typical during the coldest season with higher OA emissions from RWB. Our study's results are highly significant regarding air pollution, optical properties, and climate impact. The findings suggest that there may be an underestimation of RWB emissions in rural Europe and that further investigation is necessary.

1 Introduction

Burning woody biomass for heating and cooking has progressively increased in recent decades. Between 2009 and 2015, this increment was 34% in Europe (Camia et al., 2021). Government incentives to use "renewable" energy sources to cut fossil fuel dependence and reduce greenhouse gas emissions have contributed to this rise. In addition, the use of residential wood burning (RWB) as an energy source is significantly growing in urban and rural areas due to higher energy costs and uncertainties from the current geopolitical instability. In the winter of 2023-2024, the increasing cost of natural gas is expected to boost RWB in the region, where private households account for more than 40% of the total wood consumption for energy use (UNECE, 2022).

RWB emissions significantly contribute to ultrafine (UFP, $< 100\text{ nm}$) and fine ($< 2.5\text{ }\mu\text{m}$) aerosol particle emissions (Casquero-Vera et al., 2021; Ozgen et al., 2017). The composition of these aerosol particles includes substantial fractions of organic aerosols (OA) and black carbon (BC) (Fine et al., 2001; Liang et al., 2021). During winter, biomass burning is the principal source of primary OA emissions in the region, and, together with solid biofuels and coal combustion, it is also a primary source of BC (European Environmental Agency, 2020; Herich et al., 2014). Global emission inventories indicate that residential biomass burning produces 35% of BC emissions, occupying an important position above other emission sources, such as on-road diesel vehicle emissions (26%) (Xu et al., 2021).

The above figures are of major concern due to the adverse effects of high-content OA and BC particles on human health and climate. Black carbon has been linked to increased morbidity and mortality (Geng et al., 2013) since it carries toxic substances affecting the immune and respiratory systems as well as cardiac function (Janssen et al., 2011). Fine and ultrafine aerosol particles are potentially harmful because their size allows them to penetrate deeper into the respiratory tract and are associated with proinflammatory effects on human cells (Corsini et al., 2017; WHO et al., 2012). Organic aerosols have been connected to cardiovascular and respiratory affectations (Mauderly and Chow, 2008). The OA heterogeneous composition includes



65 Polycyclic Aromatic Hydrocarbons (PAHs), some of which have carcinogenic, mutagenic, and genotoxic properties (Chowdhury et al., 2022; Vicente and Alves, 2018, and references therein).

On the other hand, OA and BC have direct and indirect impacts on climate. Black carbon particles alter the Earth's radiative balance due to their capacity to absorb solar radiation, leading to a direct warming effect on the atmosphere (Bond et al., 2013). Indirect effects include altering lifetime and cloud formation processes since the aerosol particles can act as cloud condensation nuclei and alter the cloud mixing state (Chen et al., 2018; Koch et al., 2011). In the case of OA, these were historically considered as scattering compounds responsible for an atmospheric cooling effect; nevertheless, more recent studies evidence the warming capacity from the absorbing carbonaceous fraction present in the OA, named brown carbon (BrC) (Laskin et al., 2015, and references therein). Often, organic aerosols coating BC particles enhance the light absorption called the "lensing effect," which varies along the visible and infrared spectrum (Chen and Bond, 2010; Kalbermatter et al., 2022). Furthermore, BrC absorbs light in the shorter UV and visible wavelengths, and its inclusion in climate models has shown that the direct OA radiative forcing at the top of the atmosphere turns from cooling (negative) to warming (positive) (Feng et al., 2013).

The OA contribution to atmospheric warming processes is still being discussed. The aerosol light absorption attributed to OA (BrC) and its radiative forcing effects vary regionally depending on the emission source and the atmospheric and burning conditions. In an urban Indian site, Shamjad et al. (2016) found that BrC emissions contributed 28.5% of the total light absorption at 405 nm; in multiple locations all over France, Zhang et al. (2020) found BrC contributions ranging from 18 to 42% at 370 nm; for eastern China, Wang et al. (2018) reported a range of 10 to 24% (33% maximum) as the contribution of BrC to the total aerosol light absorption at 370 nm. The regional variability in the OA optical properties represents a challenge for global climate models and makes the constraint of the net global warming or cooling effects difficult from residential burning emissions (Kodros et al., 2015; Szopa et al., 2021). These facts show the need for source-oriented and highly temporally resolved field studies, especially in poorly characterized rural areas with significant RWB emissions, whose impacts can be underestimated (Vicente and Alves, 2018; Zhang et al., 2020).

In this work, the authors present the results of a field campaign performed in a European rural site with substantial RWB emissions. We evaluated the optical properties (light absorption coefficients (b_{abs}), mass absorption cross-section (MAC), and absorption Ångström exponent (AAE)) of the aerosol particles produced by a predominant aerosol source in an isolated village. The atmospheric stability during wintertime and the topography of the area favor the accumulation of locally produced pollutants and reduce the influence of external aerosol sources. Such circumstances allowed us to characterize aerosols produced by RWB under real conditions. Ultimately, we present the results from simple forcing efficiency estimations for the strongly light-absorbing BrC produced by RWB in the study site. We incorporated the measured optical properties in the simple forcing efficiency (SFE) calculations and compared the results by considering the OA as absorbing and non-absorbing species in the net radiative forcing (warming vs. cooling effect) over two types of surfaces (snow and Earth-average).



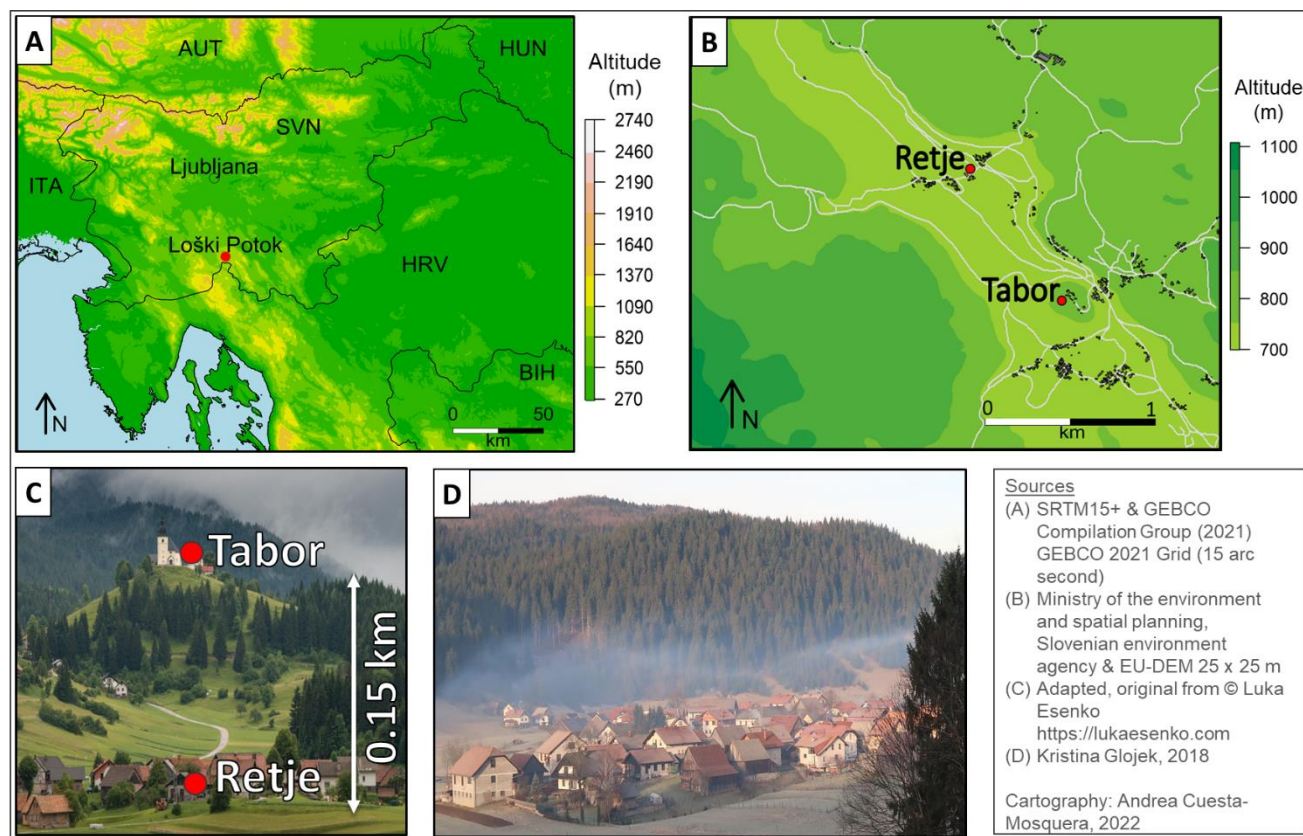
2 Methods

2.1 Study site and monitoring campaign

The field study was performed in the municipality of Loški Potok, Slovenia, in the rural village of Retje. The area is a small and shallow depression (area = 1.5 km², depth = 150 m, 45°42'34.8"N, 14°34'53.8"E, Fig. 1). The basin-shaped topography of the site favors the formation of near-ground temperature inversions, especially in the coldest season, contributing to the accumulation of atmospheric aerosols emitted locally (Glojek et al., 2022). During temperature inversions, the denser and cooler air remains at the bottom of the depression, stopping the mixing with warmer air at the top and inhibiting the vertical dilution of air pollutants.

The small village, with 690 inhabitants and 243 households, is encircled by a densely forested area; the local families use wood as the primary energy source for residential heating and cooking in the coldest season. The influence of aerosol traffic emissions is significantly low on the site, with an average of less than 100 vehicles circulating daily. The impact of industrial emissions is negligible since the nearest atmospheric industrial emission sources are more than 10 km from the monitoring site (Glojek et al., 2020, 2022).

The local topography, the atmospheric stability, and the distinctive and predominant source of aerosol emissions make Retje a unique field laboratory to investigate the optical properties of organic aerosols and black carbon produced by residential wood burning under realistic conditions. The campaign was performed during wintertime from 01 December 2017 to 07 March 2018. We used a "twin monitoring scheme" with two fixed monitoring stations operating simultaneously (Fig. 1 and Table 1). One station was located at the bottom of the hollow in the middle of the village (main station, 715 m a.s.l.), while the second station was located at Tabor hill (815 m a.s.l.) and served as a background station.



115

Figure 1: Study site and the surrounding environment: (A) geographical location in Europe, (B) geographical location of the monitoring stations in Loški Potok, (C) photo of the valley and the monitoring stations, (D) photo of Retje during a near-ground temperature inversion (27 January 2018).

2.2 Instrumentation

120

In both monitoring stations, the optical attenuation coefficient at seven wavelengths was continuously measured using filter-based absorption photometers (Aethalometers AE33, 370 to 950 nm, Aerosol Magee Scientific). The AE33s used filter tapes model M8060, made of PET polymerized polyester (59%) and fiberglass (41%). The particle number concentration (N) and particle number size distributions (PNSD) were monitored at Retje (10-800 nm) and Tabor hill (10-600 nm) using Mobility Particle Size Spectrometers (MPSS). At the village, a reference MPSS (TROPOS Ref. No. 1, high-voltage supply of positive polarity) set up with a bipolar diffusion charger (radioactive source: 85 Kr), a Differential Mobility Particle Sizer (DMA, Hauke medium), and a butanol-type condensation particle counter (CPC, TSI model 3772) operated. Whereas, at the background station, a TSI MPSS (high-voltage supply of negative polarity) set up with a bipolar diffusion charger (radioactive source: x-ray), a DMA (TSI 3081), and a water-type CPC (TSI model 3785) was installed. A multiple-charge inversion routine was applied to the raw mobility distributions to calculate the final PNSD; additional corrections were applied to the PNSD,

125



130 including CPC counting efficiency, and particle losses due to diffusion in the inlet and sampling tubes and internal particle
diffusion (corrected via the "equivalent pipe length" method, Pfeifer et al., 2014; Wiedensohler et al., 2012).
Filter samples of particulate matter were collected every 12 hours at the village station (06:00 to 18:00 and 18:00 to 06:00,
local time), using a high-volume sampler (DHA-80, Digital) to determine PM₁₀ mass concentrations (EN 12341 standard). The
quartz fiber filters were preheated before sampling and were frozen after sampling until their characterization in the laboratory.
135 The filters were analyzed to estimate the mass concentrations of elemental carbon (EC) and organic carbon (OC) (EUSAAR-
2 Protocol, (Cavalli et al., 2010)), as well as ions (NH₄⁺, Cl⁻, Na⁺, K⁺, Mg²⁺, and Ca²⁺), sugars (inositol, erythritol, levoglucosan,
arabitol mannosan, mannitol, glucose, and galactose), and salts (nitrate, sulfate, and oxalate). The total carbon (TC) mass
concentration at the village station was also measured using an online Total Carbon Analyzer (TCA08, Magee Scientific).
Cyclones with PM_{2.5} cut-off were used to sample aerosols for the AE33, MPSSs, and TCA; Nafion®Permapure air dryers
140 (length=1.5 m) kept the relative humidity of the AE33 and MPSS samples below 40%. The DHA-80 high-volume sampler
was equipped with a PM₁₀ impactor-type inlet. Table 1 shows the specifications and operating conditions of the instruments
used during the campaign. The MPSS, DHA-80, and TCA operation principles are described in the supplementary material.
The quality of the instrument measurements was assured by intercomparison, calibration, and maintenance in the laboratory.
The TROPOS Ref. No. 1 MPSS and the TSI MPSS were calibrated and intercompared against a reference MPSS (TROPOS
145 Reference MPSS No.4, set up with a CPC TSI model 3772) and a reference CPC (TSI CPC, model 3010) at the World
Calibration Center for Aerosol Physics (WCCAP) in Germany. The comparison against the reference MPSS and CPC showed
acceptable deviations within the range of ±10% for the mean particle size distributions and the integrated number of particle
concentrations). Further detailed results from the intercomparisons are shown in (Glojek et al., 2020, 2022). The AE33 and the
TCA were maintained as the manufacturer indicated (Magee Scientific, 2018, 2022), including verification and inspection of
150 the inlet flow and sampling lines, flow verification and calibration, and leakage tests.

The Aethalometer AE33 and multiple scattering harmonization

The Aethalometer AE33 collects aerosol particles in a filter matrix with a high time resolution (1 sec or 1 min). The instrument
measures the change in the light transmitted through the filter loaded with aerosols (light attenuation) due to light absorption
155 and scattering from the particles and the filter material. The AE33 creates two sample spots on the filter, which allows the
online correction of the so-called *filter-loading effect*, an artifact caused by the reduced sensitivity to detect changes in the
light attenuation produced by the accumulation of particles during sampling. More details about the AE33 algorithm and the
loading compensation can be found in Drinovec et al. (2015) and the Supplement.

The internal algorithm of the AE33 converts the attenuation change ($\Delta\text{ATN}_1(\lambda)$) into a light absorption coefficient ($b_{abs}(\lambda)$)
160 using a correction factor to account for the multiple scattering of light (C factor, Eq. S1). Multiple studies point out that the
scattering of light in filter-based absorption photometers is affected by the aerosol particles deposited on the filter matrix and
their single scattering albedo (Ajtai et al., 2019; Bernardoni et al., 2021; Collaud Coen et al., 2010; Drinovec et al., 2022; Yus-
Díez et al., 2021), together with a contribution from the filter fibers. The use of unrepresentative scattering correction factors



might lead to an overestimation of the aerosol absorption in the AE33. Therefore, the values of $b_{abs}(\lambda)$ obtained from the instrument must be corrected when using the default C given by the manufacturer. Such correction can be done using a scaling or harmonization factor obtained by collocated measurements of an Aethalometer AE33 and other instruments free of scattering artifacts, e.g., the Multi-Angle Absorption Photometer (MAAP). The Aerosol, Clouds and Trace Gases Research Infrastructure (ACTRIS) has calculated a harmonization factor (H) of 1.76 for AE33 light-absorption coefficients measured using the filter tape M8060 (for $C = 1.39$). This H -value was calculated as a European average from simultaneous AE33-MAAP measurements in rural and urban environments in the region; it is currently a recommendation from ACTRIS to the network associates, and the manuscript on this topic is in preparation. In the present study, we have used a harmonization factor to scale the light absorption coefficients from Loški Potok. Due to the absence of complementary absorption measurements in the study site, a value of $H = 1.9$ was taken from the comparison AE33-MAAP in the village of Melpitz, Germany, during winter, a rural location where RWB is a significant source of BC and OA aerosols in the coldest season (see more details in section 1.1 in the Supplement). For Loški Potok, the values of $b_{abs}(\lambda)$ obtained from the Aethalometer were harmonized as follows:

$$b_{abs}(\lambda)^{Harm.} = \frac{b_{ATN}(\lambda)}{C \cdot H} = \frac{b_{abs}(\lambda)}{H} \quad (1)$$

180 **Table 1. Instrumentation and operating conditions.**

Measurement	Instrument and manufacturer	Operating conditions	
		Time resolution	Configuration
Village (foreground) station			
Particle number size distribution (particles cm^{-3})	Mobility particle size spectrometer MPSS, TROPOS Ref. No. 1 with TSI CPC (condensation particle counter) model 3772	5 min	Sheath air to aerosol flow ratio: 5:1 L min^{-1} Radioactive source: ^{85}Kr Aerodynamic diameter range: 10-800 nm
Aerosol light absorption (Mm^{-1})	Aethalometer, model AE33, Magee Scientific	1 min	Air flow rate: 5 L min^{-1} Filter tape: M8060 $C_{M8060} = 1.39$, harmonization factor = 1.9 λ : 370, 470, 520, 590, 660, 880 & 950 nm



PM ₁₀ mass concentration (µg m ⁻³)	High-volume PM sampler, model DHA-80, DIGITEL	12 h	Air flow rate: 500 L min ⁻¹
Total carbon mass concentration (µg m ⁻³)	Total Carbon Analyzer, model TCA-80, Magee Scientific	1 h	Air flow rate: 16.7 L min ⁻¹ (Sample airflow), 0.5 L min ⁻¹ (Analytic airflow)
Temperature (°C), relative humidity (%), atmospheric pressure (mbar)	Meteorological sensor, TPR 159, AMES	1 min	--
Tabor (background) station			
Particle number size distribution (particles cm ⁻³)	Mobility particle size spectrometer MPSS, TSI Inc. with TSI CPC model 3785	5 min	Sheath air to aerosol flow ratio: 4.1:1 L min ⁻¹ Radioactive source: x-ray Aerodynamic diameter range: 10-600 nm
Aerosol light absorption (Mm ⁻¹)	Aethalometer, model AE33, Magee Scientific	1 min	Air flow rate: 5 L min Filter tape: M8060 C _{M8060} = 1.39, harmonization factor = 1.9 λ: 370, 470, 520, 590, 660, 880 & 950 nm
Temperature (°C), relative humidity (%), atmospheric pressure (mbar)	Meteorological sensor, TPR 159, AMES	1 min	--

2.3 Hourly OA and BC mass concentrations

The PM₁ mass concentration was defined as the sum of BC, OA, and inorganic aerosols (InA) masses, similar to Setyan et al. (2012). Accordingly, the hourly OA mass concentration was calculated using a mass balance as follows:

$$[OA] = [PM_1]_{MPSS} - [eBC]_{AE33} - [InA]_{Fraction\ in\ PM}, \quad (2)$$

For the previous calculation, we considered the good agreement between the PM₁₀ mass concentrations from the filters and the 12-hour averages of PM₁ from the MPSS (see Fig. 2, orthogonal fit: slope = 0.9, R² = 0.96). The comparison PM₁-PM₁₀

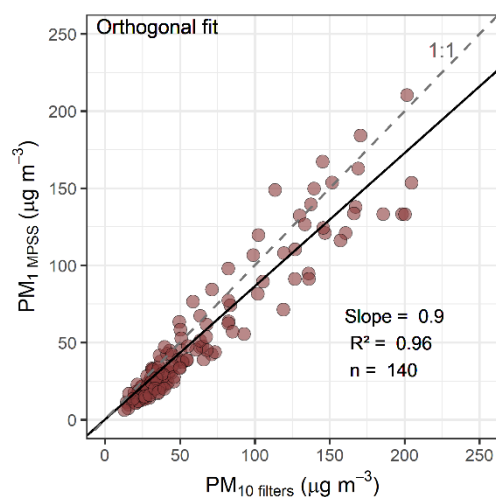


190 suggests that most of the PM_{10} is composed of PM_1 (~90 %). This approach, however, could be the largest source of uncertainty
in determining the hourly OA mass concentration since a fraction of OA might fall in the 1-2.5 microns size range; in contrast,
the fraction of BC is most probably below the PM_1 fraction. The hourly PM_1 mass concentration was estimated from the MPSS
volume size distribution, with the following assumptions: (i) the bulk aerosol density is constant ($\rho = 1.4 \text{ g cm}^{-3}$, a typical value
attributed to aerosols with relatively larger fractions of organic species (Rissler et al., 2014; Turpin and Lim, 2001)), and (ii)
195 the aerosol particles have spherical shape (the mobility diameter is equivalent to the volume-equivalent diameter). The BC
mass concentration was estimated from the optical measurement of absorption from the Aethalometer AE33, denoted
consequently as equivalent black carbon (eBC) (Petzold et al., 2013). The local mass absorption cross-section for BC (MAC_{BC})
was determined as the slope from the orthogonal fit between the 12-hour averaged aerosol light absorption at 950 nm from the
AE33 ($b_{abs}(\lambda)$) and the EC mass concentration derived from the thermo-optical analysis of the PM_{10} filters (see section 3.2.3).
200 Despite the differences between BC and EC given by their operational definitions (Bond and Bergstrom, 2006; Petzold et al.,
2013), we assume, for this study, that both species are comparable and that at 950 nm BC dominates the light absorption
(Zanatta et al., 2016). Accordingly, the eBC mass was calculated as follows:

$$eBC = \frac{b_{abs}(950 \text{ nm})^{Harm.}}{MAC_{BC}(950 \text{ nm})}, \quad (3)$$

205

The mass fraction of InA in PM_{10} (Cl^- , NH_4^+ , NO_3^- , SO_4^{2-} , $C_2O_4^{2-}$, Na, K, Mg, and Ca) was, on average, 15% of the total PM
mass. For PM_1 , we assumed a similar percentual contribution of InA considering the correlation between PM_{10} and PM_1 (see
Fig. 2) and a homogeneous distribution of the inorganic aerosols in the PM mass.



210 **Figure 2: Scatter plot and orthogonal regression (solid black line) for the PM_1 calculated from the MPSS and the PM_{10} mass from filters.** The figure includes the regression slope, the coefficient of determination (R^2), and the number of observations (n). The intercept was forced through zero.



215 The local OA/OC ratio ranged between 0.8 and 4.4, with a mean value of 1.9 ± 0.5 (see Fig. S1). OA/OC was calculated by dividing the 12-hour averaged OA_{MPSS} , by $OC_{filters}$. The estimated hourly OA mass concentration (OA_{MPSS}) was compared to the OA mass from the Total Carbon Analyzer OA_{TCA} using the local median OA/OC ratio (see Eq. S4 in the Supplement). A good agreement was observed among both variables (see Fig S2, slope = 0.92, $R^2 = 0.96$).

2.4 Simple radiative forcing efficiency

220 To estimate the climate impact of the RWB aerosol particles emitted in Retje, we used the simple forcing efficiency (SFE), which quantifies the perturbation of the emitted aerosol particles on the radiative balance of the Earth's atmosphere (Chen and Bond, 2010; Choudhary et al., 2021). For this purpose, the equation proposed by Chen and Bond (2010) was used:

$$\frac{dSFE}{d\lambda} = -\frac{1}{4} \frac{dS(\lambda)}{d\lambda} \tau_{atm}^2 (1 - F_c) [2(1 - a_s)^2 * \beta(\lambda) * MSC(\lambda) - 4a_s * MAC(\lambda)], \quad (4)$$

225 where SFE is given in $W g^{-1}$, $dS(\lambda)/d\lambda$ is the solar irradiance ($W m^{-2} nm^{-1}$) obtained from the reference solar spectra from ASTM G173-03, τ_{atm} and a_s are the atmospheric transmission (0.79) and the surface albedo (Earth average = 0.19, fresh snow = 0.80), respectively, whose values were taken from the study of Chen and Bond (2010). F_c is the cloud fraction (assumed 0.6), $\beta(\lambda)$ is the light backscatter fraction, and $MAC(\lambda)$ and $MSC(\lambda)$ are the mass absorption and mass scattering cross-sections ($m^2 g^{-1}$), respectively.

230 $\beta(\lambda)$ was estimated by the mathematical relation with the asymmetry parameter $g(\lambda)$ proposed by Sagan and Pollack (1967):

$$\beta(\lambda) = \frac{1}{2} (1 - g(\lambda)), \quad (5)$$

Mie modeling

235 The $g(\lambda)$ and $MSC(\lambda)$ were estimated using the core-shell Mie theory (Bohren and Huffman, 1998). The aerosol particles are considered to be spherical, consisting of a BC core surrounded by OA and InA, which are homogeneously mixed in the shell. As input for the Mie modeling, we provided: volumetric fractions, complex refractive indexes, and size distributions of the three components every 12 hours. The volumetric fractions were calculated considering the mass concentrations of OA, EC, and InA from the PM_{10} filters and densities from the literature (Eq. S6-S9): $\rho_{BC} = 1.8 g cm^{-3}$, $\rho_{OA} = 1.4 g cm^{-3}$, and $\rho_{InA} = 2.1 g cm^{-3}$ (Bond and Bergstrom, 2006; Li et al., 2016; Turpin and Lim, 2001). The wavelength-dependent complex refractive indexes (n -real part and k -imaginary part) of BC, OA, and InA were also taken from previous studies and are shown in Table S1 (Chen and Bond, 2010; Kim et al., 2015). Finally, the effective complex refractive index of the shell was calculated using a volume mixing rule (Eq. S10). The $MAC(\lambda)$ for the simulated core-shell particles were calculated using field measurements of particle mass and absorption, as follows:



$$MAC(\lambda) = \frac{b_{abs}(\lambda)}{PM_1}, \quad (7)$$

245 2.5 Atmospheric stability

The different categories of atmospheric stability in Loški Potok were identified according to the potential temperature gradient ($\partial\theta/\partial z$), expressed in $K\ m^{-1}$ and calculated as the difference of the absolute potential temperature (θ) from both sites (Eq. 2): Tabor hill at the top of the valley ($\theta_{background}$) and the Retje village at the bottom ($\theta_{village}$). Using the potential temperature is advantageous since it discounts the compressibility effect caused by the air pressure. θ is the temperature a parcel of air would have if it expands or compresses adiabatically (no heat is added or subtracted) and is brought to a reference pressure (Hartmann, 2016). Hourly values of θ for Retje and Tabor were calculated as shown in Eq. 3, using the measurements from the meteorological sensors operating during the campaign (Table 1).

$$\frac{\partial\theta}{\partial z} = (\theta_{background} - \theta_{village}) / dz \quad (2)$$

255

$$\theta = T * \left(\frac{P_0}{P}\right)^{R/Cp}, \quad (3)$$

260

where T is the absolute temperature, P_0 is the reference pressure (standard atmospheric pressure, 1 atm), P is the local pressure, R is the gas constant for air, and Cp is the specific heat capacity of air at constant pressure ($R/Cp = 0.286$ for ambient air (Wallace and Hobbs, 2006)).

265

The categories of atmospheric stability are given according to $\partial\theta/\partial z$: When $\partial\theta/\partial z > 0$, the potential temperature increases with height, the atmosphere is stable, and near-ground temperature inversions occur; when $\partial\theta/\partial z = 0$, the potential temperature is uniform, there are no net upward or downward buoyancy forces and the atmosphere is neutral; when $\partial\theta/\partial z < 0$, there is a decrease in the potential temperature, the atmosphere is unstable and vertical motions within an air parcel are favored (Hartmann, 2016). During the unstable conditions at Loški Potok, $\partial\theta/\partial z$ ranged from $-5\ K\ m^{-1}$ to $0\ K\ m^{-1}$, while for stable conditions $\partial\theta/\partial z$ ranged from $0\ K\ m^{-1}$ to $10\ K\ m^{-1}$. The wide range of positive $\partial\theta/\partial z$ motivated us to partition the inversion periods into two subcategories: weak inversion and strong inversion. The final categories of atmospheric stability used in the analysis are:

Table 2. Categories of atmospheric stability according to the potential temperature gradient.

Atmospheric stability	Potential temperature gradient ($K\ m^{-1}$)
Weak inversion	$0 < \partial\theta/\partial z < 2$
Strong inversion	$\partial\theta/\partial z > 2$
Unstable	$\partial\theta/\partial z < 0$
Neutral	$\partial\theta/\partial z = 0$



270 Figure S3 shows the relative frequency of the hourly atmospheric stability categories at Loški Potok during the campaign period.

2.6 Data processing and analysis

Deming's total least squares regression was used to compare measurements from different methods or instruments, estimate the mass absorption coefficients (MAC), and evaluate correlations among variables (R package "deming" Therneau, 2018).

275 Deming regression fits a couple of variables considering the independent measurement errors of both X and Y. The errors are assumed to be normally distributed, and the error ratio (E_{ratio}) is constant (Deming, 1943). For $E_{\text{ratio}} = 1$, the regression results are equivalent to the orthogonal regression. Measurement data and calculations were processed in the software R version 4.0.0 (R Core Team, 2020).

3 Results and Discussion

280 3.1 Aerosol accumulation driven by atmospheric stability

Extremely high values for aerosol mass and particle number concentrations and light absorption coefficients were measured in Retje, Loški Potok, under conditions of near-ground temperature inversion. Figure 3 shows the time series of the OA and BC mass concentrations (Fig. 3a and Fig.3b), the total light absorption coefficient at 370 nm (Fig. 3c), and the particle number size distribution (Fig. 3f) from the campaign period. For conditions of strong inversion, the OA and BC concentrations ranged from 1.9 to 271.9 $\mu\text{g m}^{-3}$ and 0.1 to 24.3 $\mu\text{g m}^{-3}$, respectively. In contrast, when the atmosphere was unstable, the OA and BC fluctuated from 0.2 to 115.2 $\mu\text{g m}^{-3}$ and 0.0 to 8.1 $\mu\text{g m}^{-3}$. The total light absorption coefficient at 370 nm reached 1103.9 Mm^{-1} under strong inversion, while the maximum value registered under an unstable atmosphere was 315.0 Mm^{-1} . The total particle number concentration (10–600 nm) peaked at its maxima of 53.5×10^3 particles cm^{-3} under strong inversion, compared with the maximum concentration of 49.3×10^3 particles cm^{-3} for unstable atmosphere (see Table 3).

285 Table 4 shows the statistical summary for the PM_{10} , EC, OC, and levoglucosan mass concentrations. For these, the 12-hour predominant atmospheric stability was also identified for periods from 06:00 to 18:00 and from 18:00 to 06:00 LT. During periods when strong inversions prevailed, the mass concentrations of PM_{10} , OC, and EC were the highest, reaching 204.7 $\mu\text{g m}^{-3}$, 93.7 $\mu\text{g m}^{-3}$, and 15.3 $\mu\text{g m}^{-3}$, respectively. The wood-burning tracer levoglucosan also exhibited higher concentrations during predominant temperature inversion periods, reaching up to 16.6 $\mu\text{g m}^{-3}$.

295 The 1-hour- and 12-hour measurements showed decreased values during weak inversion, neutral, and unstable atmosphere periods. Tables 3 and 4 show the statistical summaries of the aerosol measurements by categories of atmospheric stability and for the entire campaign period.

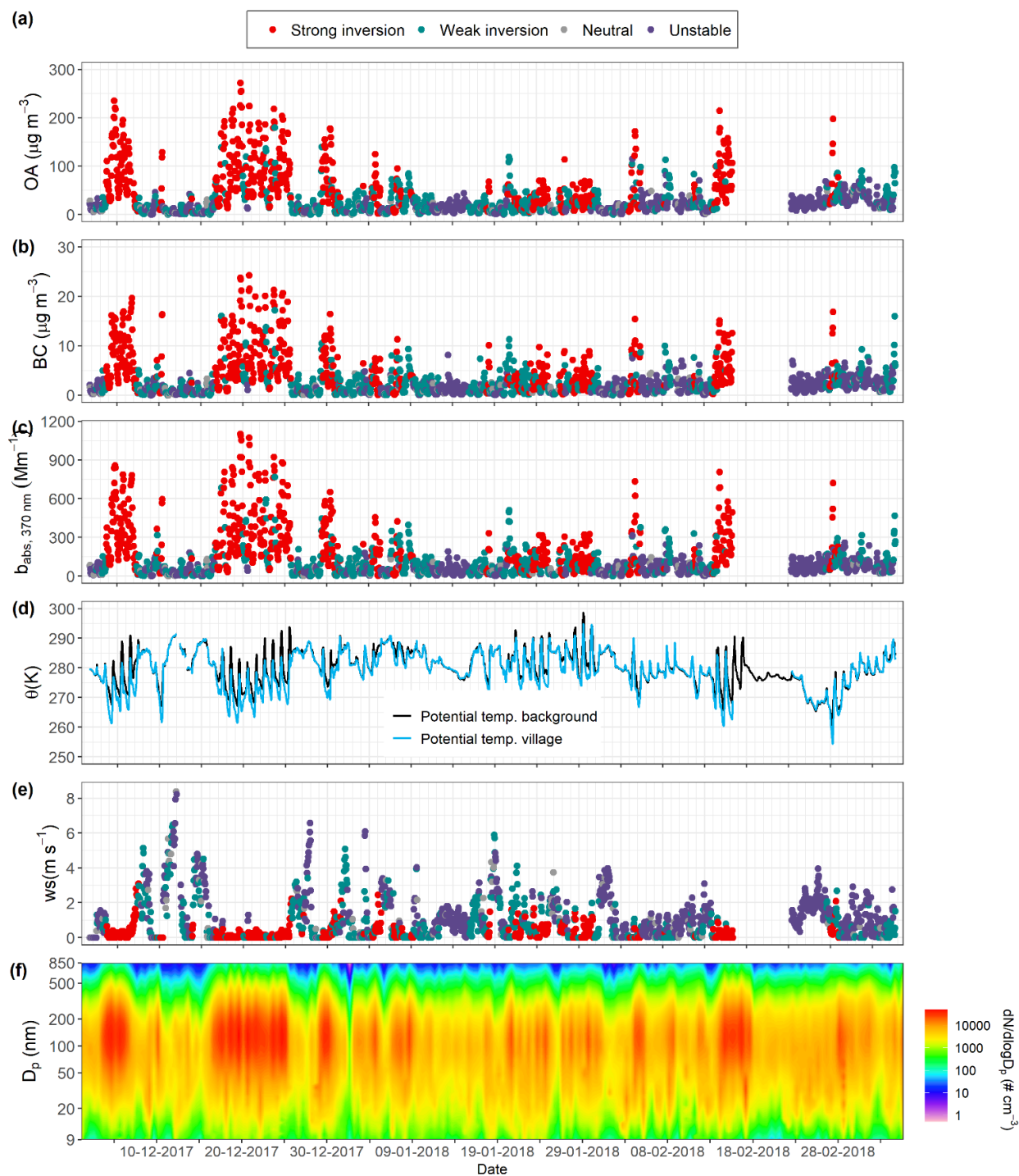


Figure 3: Time series of 1-hour organic aerosol (a) and black carbon (b) mass concentrations, (c) light absorption coefficient at 370 nm, (d) potential temperature at Retje (village) and the background, (e) wind speed, and (f) particle number size distribution at Retje.

300

Episodes of strong temperature inversion are of primary interest in this study since they favor the accumulation of aerosol particles produced by a predominant source: RWB. Presumably, the concentrations measured in the village at the bottom of the hollow are less impacted by external aerosol sources under temperature inversion. Therefore, its characterization gives an authentic fingerprint of residential wood burning emissions in a real environment. Strong and weak temperature inversion appeared 28% and 31% of the time based on hourly measurements, respectively. The more extended episodes of prevailing thermal inversion occurred from 03 to 07 December 2017, 17 to 26 December 2017, 29 December 2017 to 01 January 2018, and 14 to 17 February 2018.

The effect of atmospheric stability on the accumulation of aerosol particles in the hollow is observed when comparing the village and the background measurements. Figures 4 and 5 show the differences (Δ) in the particle number (N) and aerosol mass concentrations by atmospheric stability. The values of ΔN are, in general, positive and largest under strong inversion, while the lowest and closer to zero values were observed for unstable atmosphere. From Fig. 4, it is evident the significant contribution of RWB emissions for particles in the size range of 50 to 150 nm, with a median $\Delta N_{50-150} = 47.2 \times 10^2$ particles cm^{-3} , 22.1×10^2 particles cm^{-3} , and 14.7×10^2 particles cm^{-3} under strong inversion, weak inversion, and unstable atmosphere, respectively. In contrast, the median ΔN_{10-50} were 11.5×10^2 particles cm^{-3} , 9.8×10^2 particles cm^{-3} , and 9.6×10^2 particles cm^{-3} , and medians for $\Delta N_{150-600}$ were 2.4×10^2 particles cm^{-3} , 9.4×10^2 particles cm^{-3} , and 5.3×10^2 particles cm^{-3} , for each category of atmospheric stability, respectively.

ΔOA and ΔBC showed similar trends to ΔN . For strong inversion, weak inversion, and unstable atmosphere, the mean ΔOA was $59 \mu\text{g m}^{-3}$, $24.5 \mu\text{g m}^{-3}$, and $12 \mu\text{g m}^{-3}$, and ΔBC was $4.4 \mu\text{g m}^{-3}$, $1.5 \mu\text{g m}^{-3}$, and $0.9 \mu\text{g m}^{-3}$, respectively. In some cases, the values of ΔBC were negative, meaning the concentrations in the background were higher than in the village.

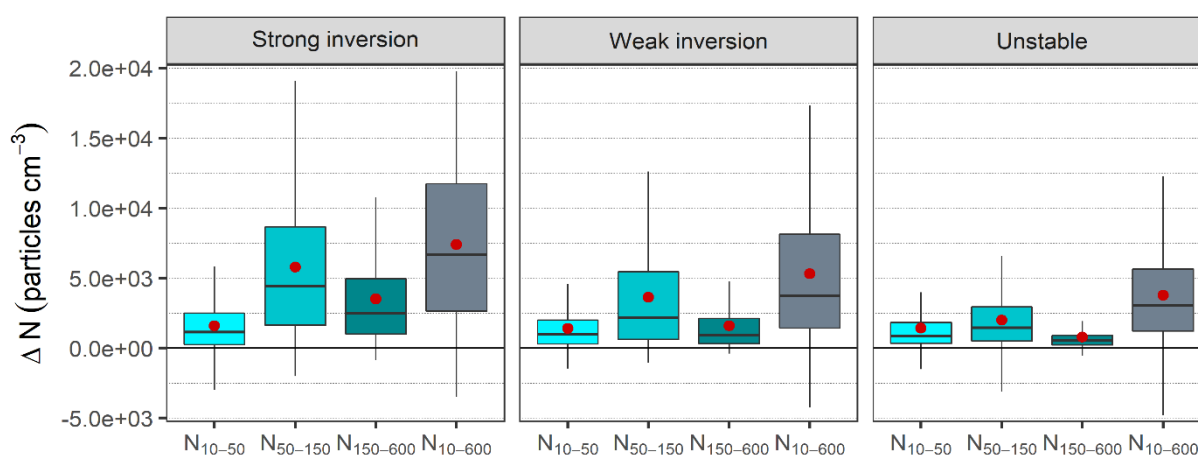


Figure 4: Boxplots and mean values (red dots) of the differences in N between the village and the background stations, according to size ranges. The maximum size range in the village was set to 600 nm to match the maximum measurement limit from the MPSS at the background station. The lower and upper borders of the boxes represent the first and third quartiles on which the middle 50% of the statistical variables are located, the black horizontal lines inside the boxes represent the median, and the whiskers represent the range of the bottom 25% and the top 25% data without outliers (black dots).

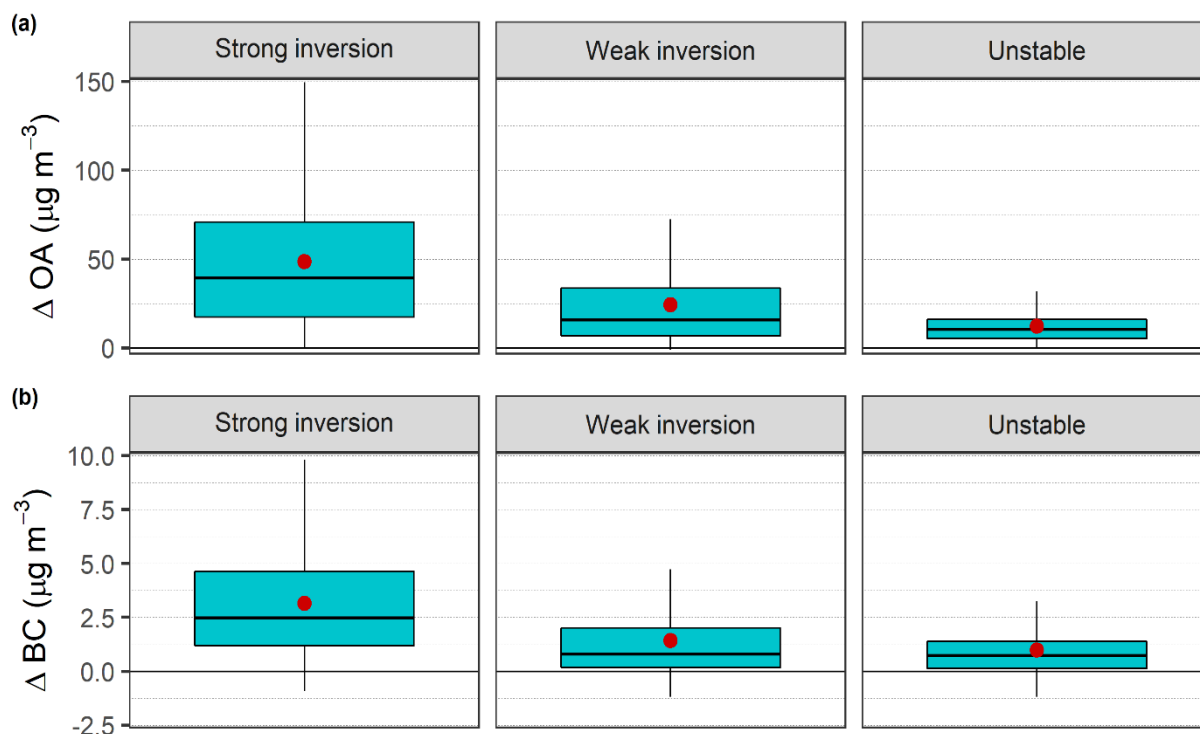


Figure 5: Boxplots and mean values (red dots) of the differences in (a) BC and (b) OA between the village and the background stations, according to atmospheric stability. The lower and upper borders of the boxes represent the first and third quartiles on which the middle 50% of the statistical variables are located, the black horizontal lines inside the boxes represent the median, and the whiskers represent the range of the bottom 25% and the top 25% data without outliers (black dots).

3.2 Aerosol optical properties

3.2.1 Light absorption coefficients

In the village, the aerosol light absorption coefficient at 370 nm ($b_{abs}(370\text{ nm})$) reached 1103.9 Mm^{-1} (under strong inversion). The total light absorption measured by the AE33 at multiple wavelengths ($b_{abs}(\lambda)$) was assumed to include the contribution of both BC and BrC. To apportion the light absorption corresponding to BC and BrC at each wavelength, we used a method based on the absorption Ångström exponent (Lack and Langridge, 2013; Massabò et al., 2015). Accordingly, for a given wavelength, we have:

$$b_{abs}(\lambda) = b_{abs,BC}(\lambda) + b_{abs,BrC}(\lambda), \quad (11)$$

For a given pair of wavelengths λ_1 and λ_2 , the mathematical definition of the BC absorption Ångström exponent (AAE_{BC}) can be written as:



$$\frac{b_{abs,BC}(\lambda_1)}{b_{abs,BC}(\lambda_2)} = \left(\frac{\lambda_1}{\lambda_2}\right)^{-AAE_{BC}}, \quad (12)$$

Taking λ_2 as 950 nm and assuming that at this wavelength the total absorption corresponds entirely to BC (the contribution from BrC is negligible), and that $AAE_{BC} = 1$, Eq. 12 is rearranged as follows,

350

$$b_{abs,BC}(\lambda_1) = b_{abs}(950 \text{ nm}) * \left(\frac{\lambda_1}{950}\right)^{-AAE_{BC} = 1}, \quad (13)$$

Combining Eq. 11 and Eq. 13, the BrC absorption at λ_1 will be:

355

$$b_{abs,BrC}(\lambda_1) = b_{abs}(950 \text{ nm}) - b_{abs,BC}(\lambda_1), \quad (14)$$

In Eq. 14 λ_1 would be any wavelength between 370 nm and 880 nm.

360

The contribution of $b_{abs, BrC}$ to the total absorption decreased toward the infrared, where the measured light absorption was assumed to be 100% from BC. The values of $b_{abs}(950 \text{ nm})$ reached 160.3 Mm^{-1} , 113.6 Mm^{-1} , and 53.6 Mm^{-1} for strong inversion, weak inversion, and unstable atmosphere, respectively.

365

A significant contribution from BrC to the total aerosol light absorption was measured in Loški Potok: during strong inversion, the average contribution of $b_{abs, BrC}$ (370 nm) was 60% (range = 17–78%, Fig. 6). For conditions of weak inversion and unstable atmosphere, the average contribution of $b_{abs, BrC}$ (370 nm) was 54% and 43%, respectively. The contribution of $b_{abs, BrC}$ to the total absorption decreased toward the infrared (470 nm = 46%, 520 nm = 37%, 590 nm = 29%, 660 nm = 18%, and 880 nm = 3%).

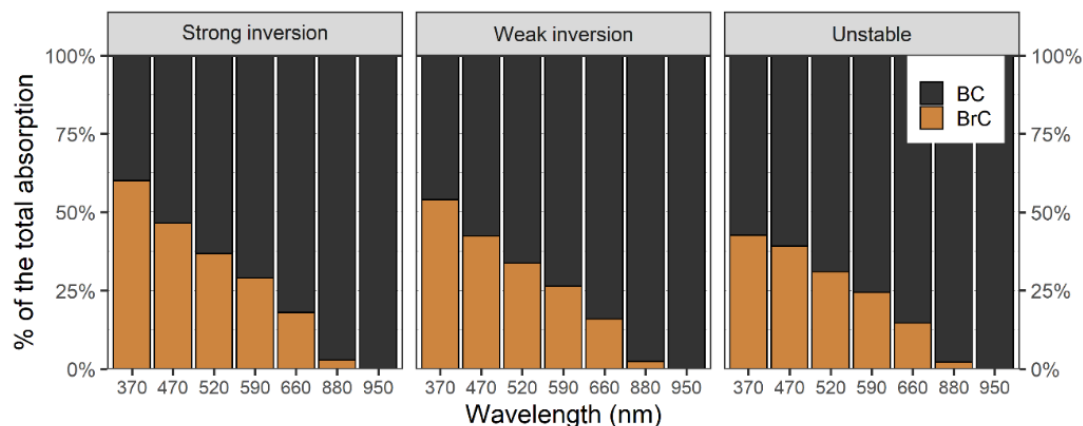


Figure 6: Mean BC and BrC contributions to light absorption from 370 nm to 950 nm in Retje, Loški Potok, according to atmospheric stability. Results for neutral atmosphere are not shown due to insufficient data.

The average contribution of BrC to the total aerosol light absorption in the near UV under strong inversion is significantly higher than findings from previous studies in urban and rural locations impacted by wood and biomass burning emissions. For instance, the national study by Zhang et al. (2020) in France found a maximum BrC contribution of 42% in the Paris area. Mbengue et al. (2021) estimated that BrC contributions in a rural and regional background station in the Czech Republic reach 19% in winter. In the Indian city of Kanpur, the mean contribution for BrC absorption was 30% (Shamjad et al., 2016). In a suburban site near Guangzhou in China, BrC contributed 24% of the total UV absorption (Qin et al., 2018). A similar and substantial contribution from BrC to the total light absorption was found in the city of Ioannina (112.400 inhabitants, (POCITYF, 2023)), Greece, where severe RWB emissions produced an average BrC contribution of 68% (calculated from the reported mean values of b_{abs} and $b_{\text{abs, BrC}}$ at 370 nm, (Kaskaoutis et al., 2022)).

3.2.2 BrC (OA) absorption Ångström exponent

The wavelength-dependence of $b_{\text{abs, BrC}}$ is plotted in Fig. 7a. Initially, a power law fit was applied to the spectral range 370–880 nm; nevertheless, we observed that the fitting curve for $b_{\text{abs, BrC}}$ throughout 370–880 nm resulted in an overestimation of the absorption at 370 nm of about ~50% (dotted grey line in Fig. 7a). Similar findings have been observed in other studies (Hoffer et al., 2006) and are associated to the presence of internally mixed aerosol particles, whose content of BrC affects the different spectral dependencies (Kumar et al., 2018). Consequently, we recalculated AAE_{BrC} for two separate ranges: 370–590 nm (more significant OA absorption) and 590–880 nm (lower OA absorption), and selected those AAE for which $R^2 \geq 0.8$. The resulting AAE_{BrC} were $\text{AAE}_{\text{BrC } 370-590 \text{ nm}} = 3.9 (\pm \text{SD } 0.4)$ and $\text{AAE}_{\text{BrC } 590-880 \text{ nm}} = 7.6 (\pm \text{SD } 0.4)$ under strong inversion (Fig. 7b and 7c). Multiple authors have addressed the sensitivity of the AAE to the range of wavelengths selected for its calculation (Harrison et al., 2013; Utry et al., 2014). Yet, the extent of this sensitivity depends on the aerosol source. It is lower for aerosols with predominant BC (Cuesta-Mosquera et al., 2021) and higher for samples containing a substantial contribution of organic species.

The median values of AAE differ by atmospheric stability (statistically significant difference, non-parametric median Mood's test, $p\text{-values} < 0.05$, $\alpha = 0.05$). Under weak inversion and unstable atmosphere, $\text{AAE}_{\text{BrC } 370-590 \text{ nm}}$ was $3.7 (\pm \text{SD } 0.5)$ and $3.5 (\pm \text{SD } 0.5)$, and $\text{AAE}_{\text{BrC } 590-880 \text{ nm}}$ was $7.8 (\pm \text{SD } 0.7)$ and $7.7 (\pm \text{SD } 1.1)$, respectively. The variation between the median AAE values amid the atmospheric stability categories suggests a slight change in the composition of the organic aerosols among the three, most likely driven by the mixing of aerosols from external sources and photochemical processes (He et al., 2022; Liu et al., 2016).

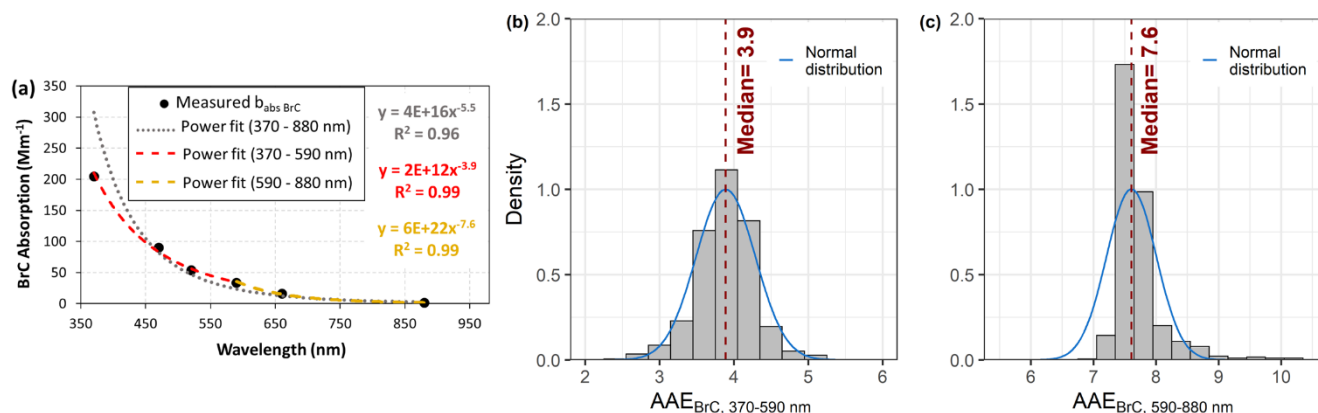


Figure 7: (a) Power law fittings of the BrC absorption spectra, (b) histogram of the BrC Absorption Ångström Exponent from 370 to 590 nm, and (c) histogram of the BrC Absorption Ångström Exponent from 590 to 880 nm.

3.2.3 BrC (OA) and BC Mass absorption cross-sections (MAC)

400 The RWB OA mass absorption cross-section (MAC_{OA}) was estimated as the slope from the fitting among the organic aerosol mass and the apportioned BrC light absorption. Figure 8a shows the scatter plot and orthogonal fitting for measurements under strong inversion (highest accumulation of OA).

For the study site, the estimated RWB MAC_{OA, 370 nm} = 2.4 m² g⁻¹ (calculated for conditions of strong inversion). For periods of weak inversion MAC_{OA, 370 nm} did almost not change (2.3 m² g⁻¹). On the contrary, for an unstable atmosphere, MAC_{OA, 370 nm} (1.8 m² g⁻¹), was lower and statistically significantly different than the MAC values calculated for strong and weak inversion (hypothesis test, *p*-value < 0.0001, α = 0.05). The decreased MAC_{OA, 370 nm} for unstable conditions, is associated with lower
 405 OA absorption. Along with little absorption, the reduced MAC_{OA, 370 nm}, indicates the presence of diverse light-absorbing compounds during an unstable atmosphere since the mixing with aerosols from external non-local sources and regionally processed aerosol is presumed.

410 Table 5 shows the spectral variation of MAC_{OA} calculated by correlating the OA mass and the BrC apportioned absorption at multiple wavelengths (370 nm, 470 nm, 520 nm, 590 nm, and 660 nm). The major MAC_{OA} value was calculated for 370 nm. We observed reduced MAC_{OA} by increasing wavelength due to decreased OA light absorption when moving toward the infrared. It was also observed that for larger wavelengths, the variability of the MAC_{OA} within the atmospheric stability categories was insignificant as *b*_{abs, BrC} approached zero.

415 The same approach was used to estimate MAC_{BC} by correlating the EC mass from filters and the 12-hour averaged absorption at 950 nm. For the study site, MAC_{BC, 950 nm} = 6.7 m² g⁻¹ (Fig. 8b). For periods of weak inversion and unstable conditions, MAC_{BC, 950 nm} was 6.5 m² g⁻¹ and 7.2 m² g⁻¹, respectively. Although the calculated MAC_{BC, 950 nm} for unstable conditions seems to be slightly higher, we found that the differences among the slopes are not statistically significant, i.e., there is no interaction effect from the atmospheric stability (strong inversion and unstable atmosphere: hypothesis test, *p*-value = 0.114, α = 0.05;
 420 weak inversion and unstable atmosphere: hypothesis test, *p*-value = 0.088, α = 0.05).



We compared our specific RWB MAC_{OA} to values reported in the literature for wood and biomass-burning emissions. In the near-UV region, the values of MAC_{OA} are spread and range between 0.2 and $5.8 \text{ m}^2 \text{ g}^{-1}$ (Table 6). Comparable results to those from Loški Potok were observed in the studies of Chen and Bond (2010) for laboratory analyses of methanol-soluble organic carbon (MSOC) from wood combustion ($MAC_{MSOC, 370 \text{ nm}} = 2.0 \text{ m}^2 \text{ g}^{-1}$) and Cheng et al. (2011) for water-soluble organic carbon extracts (WSOC) from an urban environment in Beijing impacted by biomass burning and fossil fuel emissions during winter ($MAC_{WSOC, 370 \text{ nm}} = 1.79 \text{ m}^2 \text{ g}^{-1}$). The spreading of the reported MAC_{OA} values originates in the OA nature; these are heterogeneous and non-separable mixtures of absorbing and non-absorbing materials, whose composition and physicochemical properties change depending on: (i) how the OA is constrained and measured, (ii) the burning source, (iii) the combusting conditions, (iv) the geographical location and time of measurements, and (v) the meteorological conditions. Points (iv) and (v) influence the OA aging driven by photochemical reactions in the atmosphere and the presence of aerosols from distinct combustion sources. An example to illustrate (i) refers to the unequal light-absorbing properties of the WSOC and the MSOC extracted from particulate matter filters (Chen and Bond, 2010; Kim et al., 2016; Zhu et al., 2018). In addition, whether the OA should be analyzed as a fraction or a bulk has been addressed previously and remains an open discussion (Zhang et al., 2016). These facts reinforce the necessity of performing specific and source-oriented OA characterization.

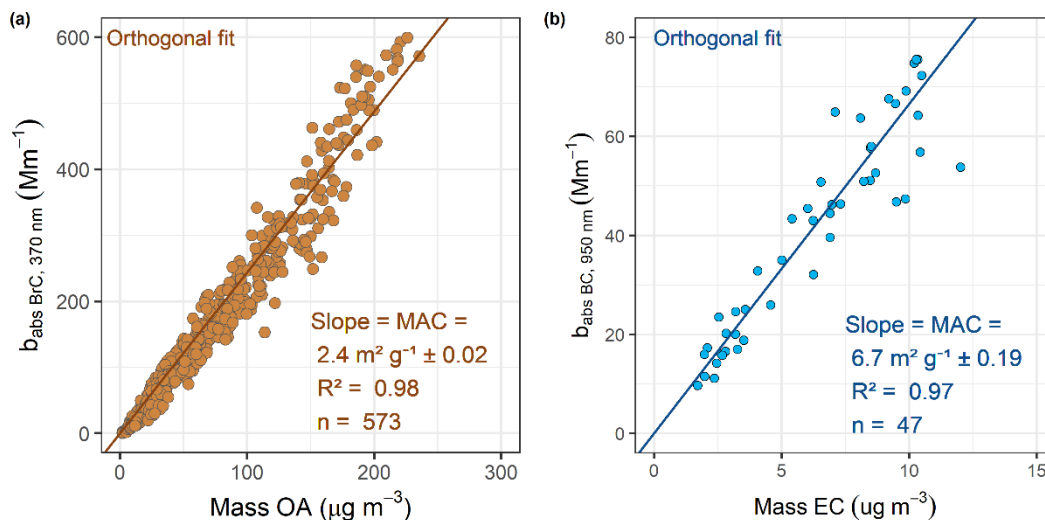


Figure 8: Scatter plots and orthogonal fits for the village measurements of (a) 1-hour BrC light absorption at 370 nm and OA mass concentrations and (b) 1-hour BC light absorption at 950 nm and EC mass concentrations under strong near-ground temperature inversion. The figure includes the regression slope \pm the standard error of the slope, the coefficient of determination (R^2), and the number of observations (n). The intercept was forced through zero.

Table 5. Spectral variation of the organic aerosol MAC by atmospheric stability.

Wavelength	$MAC_{OA} (\text{m}^2 \text{ g}^{-1})$		
	Strong inversion	Weak Inversion	Unstable
370 nm	2.4	2.3	1.8



470 nm	1.0	1.0	0.8
520 nm	0.4	0.4	0.3
590 nm	0.3	0.3	0.2
660 nm	0.2	0.2	0.1
880 nm	< 0.1	< 0.1	< 0.1
950 nm	Zero by definition		

Table 6. Comparison of light absorption properties for OA (also referred to as BrC and OC) reported in the literature.

Type of study	Reference and region	MAC ($\text{m}^2 \text{g}^{-1}$)		AAE		Type of site and main aerosol sources	
		λ (nm)	Value	λ (nm)	Value		
Laboratory	Chen and Bond, 2010	370	0.6 ^a	360-500	9.4	Wood (pine)	
			2.0 ^b		7.5		
	Olson et al., 2015	370	0.21	n.a.	n.a.	Wood pellets	
	Kumar et al., 2018	370	5.5	370, 880	4.6	Beechwood	
Field campaign	Cheng et al., 2011 (West Asia)	365	1.79	330-480	7.5	Urban; BB, FF	
	Zhang et al., 2021 (West Asia)	370	4.33	370-520	4.22	Urban; CC, FF, RWB	
	Srinivas and Sarin, 2014 (South Asia)	365	0.78	300-800	6.0	Urban; BB, RWB, FF	
	Kim et al., 2016 (East Asia)	365		0.85 ^c	300-700	5.05 ^d	Urban background; BB, FF, LRT
				1.02 ^a		7.23 ^e	
	Chen et al., 2020 (East Asia)	365		0.91 ^a	n.d.	n.d.	Urban; BB, FF, LRT
				1.05 ^b			
	Zhang et al., 2016 (North America)	405	0.60	n.d.	n.d.	Urban; BB, FF, RWB	
	Lack et al., 2012 (North America)	404	1.0	404-658	2.3	Rural; FoF	
	Hoffer et al., 2006 (South America)	n.a.	n.a.	300-700	6.4	Rural; FoF	
Liakakou et al., 2020 (South Europe)	370	4.25	370-660	3.85 ^f	Urban background; FF, RWB		
This study, 2023	370	2.4	370-590	3.9	Rural; RWB		



	(Central Europe)			590-880	7.6	
				370-880	5.5	

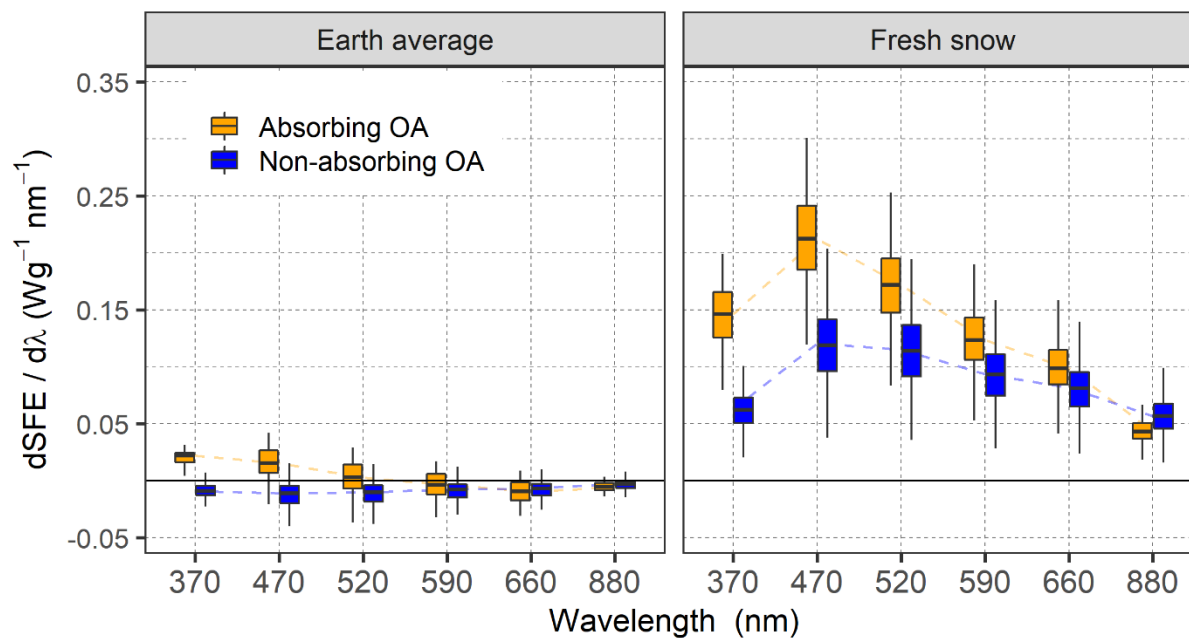
a: WSOC; b: MSOC; c: OC; d. Wavelength-dependency of the absorption measured on MSOC; e. Wavelength-dependency of the absorption measured on WSOC; f: Wintertime; BB: Biomass burning other than wood burning; CC: Coal combustion; FF: Fossil fuel; FoF: Forest fires; LRT: Long-range transport; RWB: Residential wood burning; n.a.: non-applicable data; n.d.: non-available data.

3.3 Climate impact: sensitivity analysis through simple forcing efficiency calculations

The model described in section 2.5 was used as a sensitivity analysis tool to evaluate the climate impact of the light-absorbing properties of the RWB aerosol particles at Loški Potok. The SFE represents the perturbation to the atmospheric radiative balance of the Earth by a given mass of aerosols (Choudhary et al., 2021). Figure 9 shows the spectral variation of the SFE for two different types of surfaces: fresh snow ($\beta = 0.80$) and Earth-average ($\beta = 0.19$). In each case, the forcing efficiency was calculated for two scenarios: (i) assuming OA as light-absorbing species (imaginary refractive index k_{BrC} calculated from $b_{abs, BrC}$, Eq. 8) and (ii) assuming OA as non-absorbing (imaginary refractive index $k_{BrC} = 0$). The SFE was calculated for the seven wavelengths covered by the AE33. The total radiative forcing (RF) was calculated by integrating the area under the curves using the trapezoidal rule (blue and yellow lines in Fig. 9).

The resulting SFE was larger and positive for bright snow and relatively small for the Earth-average surface. For non-absorbing OA, the SFE was lower than for absorbing with slightly negative values for the Earth-average surface. The comparison among surfaces indicates that RWB aerosols have a more significant impact over bright surfaces, for instance, the Arctic or areas covered by snow, typical during the coldest season when the largest emissions of OA are expected due to more intense RWB. We also observed that SFE is larger at 470 nm despite the significantly higher mass absorption cross-section calculated at 370 nm. This observation is attributed to the larger solar irradiance $dS(\lambda)/d\lambda$ reported in the blue region (1.1 to 1.4 W m² nm⁻¹) compared to the values from the near UV (0.0 to 0.8 W m² nm⁻¹).

For fresh snow, the corresponding RF of the RWB aerosols was 61.2 W g⁻¹ and 43.7 W g⁻¹ for absorbing OA and non-absorbing OA, respectively. For an Earth-average surface, the RF was 0.2 W g⁻¹ and -3.9 W g⁻¹ for absorbing and non-absorbing OA. The RF was two times higher for a snow-like area and passed from cooling to warming for an Earth-average surface by taking OA as light-absorbing species. Our calculations show the crucial influence of the OA in atmospheric warming via the lensing effect of coated BC and absorption in shorter wavelengths; notwithstanding, robust climate models are essential to reporting definite radiative forcing figures since these consider further atmospheric processes and aerosol properties such as aerosol-cloud interactions, aerosol hygroscopicity, and the total vertical column of aerosols.



470 **Figure 9: Spectral variation of the simple forcing efficiency of the RWB aerosols characterized at Loški Potok and comparison of results obtained from considering absorbing OA and non-absorbing OA for two types of surfaces: fresh snow and Earth-average. The yellow and blue dotted lines connect the median values of $dSFE/d\lambda$.**

Table 3. Statistics for 1-hour measurements of mass concentrations, particle number concentration, and light absorption coefficients at the village Retje, according to atmospheric stability.

Atmospheric stability	Strong inversion			Weak inversion			Neutral		
% Occurrence during the campaign	28%			31%			5%		
Measurement	Min	Max	Mean \pm sd	Min	Max	Mean \pm sd	Min	Max	Mean \pm sd
PM ₁ ($\mu\text{g m}^{-3}$)	2.4	347.8	91.1 \pm 70.8	0.4	231.9	32.4 \pm 32.7	0.8	67.5	17.34 \pm 16.0
OA ($\mu\text{g m}^{-3}$)	1.9	271.9	70.9 \pm 55.6	0.2	179.9	25.2 \pm 25.5	0.6	54.5	13.6 \pm 12.7
BC ($\mu\text{g m}^{-3}$)	0.1	24.3	6.1 \pm 5.0	0.0	17.2	2.3 \pm 2.4	0.0	4.7	1.2 \pm 1.1
TC ($\mu\text{g m}^{-3}$)	3.6	126.1	34.0 \pm 26.7	3.2	108.4	17.6 \pm 15.5	3.5	21.2	9.8 \pm 5.0
Total N ($\times 10^3 \text{ cm}^{-3}$)	1.3	53.5	17.4 \pm 11.7	0.5	58.7	8.5 \pm 7.5	0.4	17.5	4.9 \pm 3.5
$b_{\text{abs } 370 \text{ nm}}$ (Mm^{-1})	2.1	1103.9	260.6 \pm 226.1	0.2	768.9	88.9 \pm 99.3	0.7	163.3	43.4 \pm 41.4



$b_{\text{abs BrC } 370 \text{ nm}} (\text{Mm}^{-1})$	0.5	701.3	161.2 ± 144.9	0.0	477.3	50.8 ± 61.4	0.0	90.6	22.3 ± 22.6
$b_{\text{abs BC } 370 \text{ nm}} (\text{Mm}^{-1})$	1.5	411.6	99.4 ± 84.6	0.2	291.6	38.1 ± 40.5	0.4	80.3	21.1 ± 20.4
$b_{\text{abs } 880 \text{ nm}} (\text{Mm}^{-1})$	0.7	179.1	43.1 ± 36.8	0.1	127.1	16.4 ± 17.5	0.2	34.4	9.1 ± 8.8
$b_{\text{abs BrC } 880 \text{ nm}} (\text{Mm}^{-1})$	0.0	6.4	1.3 ± 1.3	0.0	4.5	0.4 ± 0.5	0.0	0.9	0.2 ± 0.2
$b_{\text{abs BC } 880 \text{ nm}} (\text{Mm}^{-1})$	0.7	173.1	41.8 ± 35.6	0.1	122.6	16.0 ± 17.0	0.2	33.8	8.9 ± 8.6

475

Table 3. (Continued) Statistics for 1-hour measurements of mass concentrations, particle number concentration, and light absorption coefficients at the village Retje, according to atmospheric stability.

Atmospheric stability	Unstable			Total period		
	36%					
% Occurrence during the campaign						
Measurement	Min	Max	Mean \pm sd	Min	Max	Mean \pm sd
PM ₁ ($\mu\text{g m}^{-3}$)	0.2	200.5	23.0 ± 18.2	0.2	347.8	44.6 ± 51.8
OA ($\mu\text{g m}^{-3}$)	0.2	115.2	17.8 ± 13.2	0.2	271.9	34.8 ± 40.8
BC ($\mu\text{g m}^{-3}$)	0.0	8.1	1.6 ± 1.3	0.0	24.3	3.1 ± 3.6
TC ($\mu\text{g m}^{-3}$)	3.1	59.5	11.9 ± 7.4	3.1	126.1	19.3 ± 18.9
Total N ($\times 10^3 \text{ cm}^{-3}$)	0.4	49.3	6.1 ± 4.8	0.4	58.7	9.9 ± 9.3
$b_{\text{abs } 370 \text{ nm}} (\text{Mm}^{-1})$	0.1	315.9	55.5 ± 44.1	0.1	1103.9	122.8 ± 160.3
$b_{\text{abs BrC } 370 \text{ nm}} (\text{Mm}^{-1})$	0.0	188.7	28.0 ± 25.1	0.0	701.3	72.2 ± 102.3
$b_{\text{abs BC } 370 \text{ nm}} (\text{Mm}^{-1})$	0.1	137.6	27.5 ± 22.2	0.1	411.6	50.6 ± 60.4
$b_{\text{abs } 880 \text{ nm}} (\text{Mm}^{-1})$	0.0	59.4	11.8 ± 9.5	0.0	179.1	21.9 ± 26.2
$b_{\text{abs BrC } 880 \text{ nm}} (\text{Mm}^{-1})$	0.0	1.6	0.3 ± 0.2	0.0	6.4	0.6 ± 0.9
$b_{\text{abs BC } 880 \text{ nm}} (\text{Mm}^{-1})$	0.0	57.9	11.6 ± 9.3	0.0	173.1	21.3 ± 25.4



Table 4. Statistics for 12-hour measurements of PM₁₀ and its composition at the village Retje, according to atmospheric stability.

Atmospheric stability	Strong inversion			Weak Inversion			Unstable			Total period		
% Occurrence during the campaign	36%			33%			31%					
Measurement	Min	Max	Mean ± SD	Min	Max	Mean ± SD	Min	Max	Mean ± SD	Min	Max	Mean ± SD
PM ₁₀ (µg m ⁻³)	28.0	204.7	111.1 ± 51.4	15.4	83.5	37.2 ± 16.8	12.9	82.3	36.5 ± 14.9	12.9	204.7	63.4 ± 48.6
EC (µg m ⁻³)	1.7	15.3	6.4 ± 3.3	0.4	5.3	2.2 ± 1.2	0.4	6.0	1.8 ± 1.2	0.4	15.3	3.6 ± 3.0
OC (µg m ⁻³)	8.6	93.7	46.8 ± 24.4	3.5	36.1	12.6 ± 7.9	2.2	24.1	9.6 ± 4.8	2.2	93.7	23.9 ± 23.1
OC/EC	3.6	12.6	7.3 ± 1.8	2.9	13.3	6.2 ± 2.2	1.7	14.3	6.2 ± 2.6	1.7	14.3	6.6 ± 2.3
Levoglucosan (µg m ⁻³)	1.1	16.6	6.7 ± 3.9	0.3	7.5	2.0 ± 1.4	0.3	2.9	1.3 ± 1.2	0.3	16.6	3.5 ± 3.5
K ⁺ (µg m ⁻³)	0.4	5.0	1.7 ± 0.9	0.1	2.2	0.6 ± 0.4	0.1	1.2	0.6 ± 0.3	0.1	5.0	1.0 ± 0.8
Cl ⁻ (µg m ⁻³)	0.07	1.5	0.4 ± 0.3	0.02	0.6	0.2 ± 0.1	0.02	0.7	0.1 ± 0.1	0.02	1.5	0.2 ± 0.2

480 4 Summary and Conclusions

Residential wood burning (RWB) is currently a significant source of OA and BC emissions; however, the net global cooling and warming effects of aerosols produced by residential biofuel burning it is still not well constrained; to undertake this challenge, further research is needed. In this context, the main focus of this study was the characterization of the aerosol particles produced by intensive RWB in a rural location in Central Europe occupied by 243 households. We evaluated the influence of atmospheric stability on aerosol accumulation, measured and calculated their optical properties using filter-based absorption photometers (Aethalometers AE33), and connected these to climate impact via simple radiative forcing estimates. Intense burning in Loški Potok, Slovenia, and near-ground temperature inversion led to a significant accumulation of aerosols produced by RWB during the coldest season at this rural site. During strong inversion, the mean OA and BC mass concentrations of $70.9 \mu\text{g m}^{-3} \pm 55.6$ and $6.1 \mu\text{g m}^{-3} \pm 5$, respectively, with maximum values of $271.9 \mu\text{g m}^{-3}$ and $24.3 \mu\text{g m}^{-3}$. The mean and maximum particle number concentrations were $17.4 \times 10^3 \text{ particles cm}^{-3} \pm 11.7 \times 10^3$ and $53.5 \times 10^3 \text{ particles cm}^{-3}$, respectively. Deplorable air quality conditions at the bottom of the valley, driven by a stable atmosphere, occurred 60% of the time in winter. The transition from a stable to an unstable atmosphere, reduced OA, BC, and particle number concentrations: from strong inversion to weak inversion and unstable atmosphere, the OA mass concentration decreased by 25% and 80%, respectively, the BC mass decreased by 62% and 74%, and the particle number concentration decreased by 50% and 65%.



Significant aerosol accumulation under near-ground temperature inversion and a presumed low mixing were used conveniently to estimate optical properties of RWB under real conditions with low influence from distinct aerosol sources. During strong inversion, the mean $b_{\text{abs, BrC}}$ and $b_{\text{abs, BC}}$ at 370 nm were 161.2 Mm^{-1} and 99.4 Mm^{-1} , respectively. Under weak inversion, $b_{\text{abs, BrC}}$ and $b_{\text{abs, BC}}$ were 69% and 62% lower, and during unstable atmosphere, 83% and 73% lower, respectively. The average contribution of BrC to the total light absorption was 60% at 370 nm during strong temperature inversion and decreased toward the infrared (470 nm = 46%, 880 nm = 3%).

The estimated MAC_{OA} for residential wood burning was $2.4 \text{ m}^2 \text{ g}^{-1}$ at 370 nm and decreased towards the infrared with values of $1.0 \text{ m}^2 \text{ g}^{-1}$, $0.4 \text{ m}^2 \text{ g}^{-1}$, $0.3 \text{ m}^2 \text{ g}^{-1}$, and $0.2 \text{ m}^2 \text{ g}^{-1}$, for 470 nm, 520 nm, 590 nm, and 660 nm, respectively. The calculated MAC_{OA} at 880 nm was below $0.1 \text{ m}^2 \text{ g}^{-1}$. The values of MAC_{OA} for Loški Potok are higher than multiple MAC_{OA} reported from urban and rural locations impacted by wood burning. Nevertheless, differences in MAC between locations are expected due to the influence of diverse aerosol sources and aerosol aging. The higher MAC_{OA} in the study site is attributed to the significant load of organic aerosols and elevated absorption coefficients measured during the campaign period. Nevertheless, the assumptions involved in the calculation of the hourly OA mass concentration are identified as the main limitation and source of uncertainty in the calculation of MAC_{OA} . Despite the good agreement found between OA_{MPSS} and OA_{TCA} , we recognize that calculating OA from the PM_{10} mass estimated from the MPSS might lead to an omission of OA fraction in the PM_{10} - $\text{PM}_{2.5}$ size range. The RWB AAE_{BrC} was 3.9 in the wavelength range of 370–590 nm. The estimated values of MAC_{OA} and AAE_{BrC} fall within the range of previously reported optical BrC optical properties (Chen and Bond, 2010; Cheng et al., 2011; Liakakou et al., 2020).

The optical properties from the study site were used to estimate SFE and RF from RWB aerosols. The large contribution of BrC to the total aerosol light absorption resulted in a substantial impact. Results showed a turn from cooling to warming for an Earth-average surface when the OA light-absorption properties were considered in the SFE modeling (i.e., the OA were not assumed to be purely scattering compounds). For a snow-covered surface, the warming RF passed from 43.7 W g^{-1} to 61.2 for absorbing and non-absorbing OA, respectively. This last observation is important since snowy surfaces are common during the coldest seasons and will probably occur in parallel with intense RWB and OA emissions. The estimated SFE and RF were significantly higher than those reported in previous studies such as Chen & Bond (23 W g^{-1} over snow and -12 W g^{-1} for an Earth average albedo, (2010)). The much larger SFE and RF calculated for Loški Potok are directly related to the substantial b_{abs} measured at the site and the relatively larger MAC, which exceeds typical values reported for other locations impacted by RWB. The SFE and RF calculations were calculated as sensitivity analysis of the aerosol light absorption effect on climate and should be taken as indicative only, due to the limitations of this approach which include the omission of aerosol hygroscopicity and further atmospheric processes that could take place. Further studies should include more complex atmospheric processes and aerosol properties to report the absolute values for a complete understanding of the climate implications.

To our knowledge, the results presented in this study, in complement to the findings of Glojek et al. (2022), are the first to show such significant pollution levels and light absorption coefficients from residential wood burning emissions in rural



530 Central Europe. Our findings suggest that the severity and impacts of rural RWB emissions on air quality and climate in the region might be underestimated and overlooked. Additional monitoring and modeling should be considered since the use of RWB is rising worldwide.

Code and data availability

The corresponding author can provide the data and the scripts used for data processing upon request.

535 **Supplement**

The supplementary material of this study is available online at:

Author contributions

540 AW, GM, LD, MO, KG, TM, and ACM conceptualized and designed the study. KG, KW, GM, LD, MO, MM, DvP, and MR set up, operated, calibrated, maintained the instruments during the field study. KG and AG performed the field measurements with support from KW. DvP and HH provided data from the characterization of the PM₁₀ filter-based measurements. BR performed the Mie modeling. ACM curated, processed, and completed the formal data analysis with inputs from KG, TM, GM, AG, and MR. ACM wrote and prepared the original manuscript draft with inputs from KG, TM, GM, and MP. All the authors reviewed, edited, and contributed to the scientific discussion in the manuscript.

Competing interests

545 The authors declare that they have no conflict of interest.

Acknowledgments

550 The authors acknowledge the financial support from the Slovenian Research Agency (program MR-2016, 680 program P1-0385 "Remote sensing of atmospheric properties"), Municipality of Loški Potok, and the COST Action CA16109 COLOSSAL. We want to thank all the people and institutes involved in the campaign. We are genuinely grateful to the local community for their friendly welcome, help, and support.

References

Ajtai, T., Kiss-Albert, G., Utry, N., Tóth, Á., Hoffer, A., Szabó, G. and Bozóki, Z.: Diurnal variation of aethalometer correction



- factors and optical absorption assessment of nucleation events using multi-wavelength photoacoustic spectroscopy, *J. Environ. Sci. (China)*, 83, 96–109, doi:10.1016/j.jes.2019.01.022, 2019.
- 555 Andreae, M. O. and Gelencsér, A.: Black carbon or brown carbon? the nature of light-absorbing carbonaceous aerosols, *Atmos. Chem. Phys.*, 6(10), 3131–3148, doi:10.5194/acp-6-3131-2006, 2006.
- Bernardoni, V., Ferrero, L., Bolzacchini, E., Corina Forello, A., Gregorič, A., Massabò, D., Mocnik, G., Prati, P., Rigler, M., Santagostini, L., Soldan, F., Valentini, S., Valli, G. and Vecchi, R.: Determination of Aethalometer multiple-scattering enhancement parameters and impact on source apportionment during the winter 2017/18 EMEP/ACTRIS/COLOSSAL campaign in Milan, *Atmos. Meas. Tech.*, 14(4), 2919–2940, doi:10.5194/amt-14-2919-2021, 2021.
- 560 Bohren, C. F. and Huffman, D. R.: *Absorption and Scattering of Light by Small Particles*, John Wiley & Sons, New York., 1998.
- Bond, T. C. and Bergstrom, R. W.: Light absorption by carbonaceous particles: An investigative review, *Aerosol Sci. Technol.*, 40(1), 27–67, doi:10.1080/02786820500421521, 2006.
- 565 Bond, T. C., Doherty, S. J., Fahey, D. W., Forster, P. M., Berntsen, T., Deangelo, B. J., Flanner, M. G., Ghan, S., Kärcher, B., Koch, D., Kinne, S., Kondo, Y., Quinn, P. K., Sarofim, M. C., Schultz, M. G., Schulz, M., Venkataraman, C., Zhang, H., Zhang, S., Bellouin, N., Guttikunda, S. K., Hopke, P. K., Jacobson, M. Z., Kaiser, J. W., Klimont, Z., Lohmann, U., Schwarz, J. P., Shindell, D., Storelvmo, T., Warren, S. G. and Zender, C. S.: Bounding the role of black carbon in the climate system: A scientific assessment, *J. Geophys. Res. Atmos.*, 118(11), 5380–5552, doi:10.1002/jgrd.50171, 2013.
- 570 Camia, A., Giuntoli, J., Jonsson, R., Robert, N., Cazzaniga, N. E., Jasinevičius, G., Avitabile, V., Grassi, G., Barredo, J. I. and Mubareka, S.: The use of woody biomass for energy production in the EU and impacts on forests The use of woody biomass for energy production in the EU., 2021.
- Casquero-Vera, J. A., Lyamani, H., Titos, G., Minguillón, M. C., Dada, L., Alastuey, A., Querol, X., Petäjä, T., Olmo, F. J. and Alados-Arboledas, L.: Quantifying traffic, biomass burning and secondary source contributions to atmospheric particle number concentrations at urban and suburban sites, *Sci. Total Environ.*, 768, doi:10.1016/j.scitotenv.2021.145282, 2021.
- 575 Cavalli, F., Viana, M., Yttri, K. E., Genberg, J. and Putaud, J.-P.: Toward a standardised thermal-optical protocol for measuring atmospheric organic and elemental carbon: the EUSAAR protocol, *Atmos. Meas. Tech.*, 3(1), 79–89, doi:10.5194/amt-3-79-2010, 2010.
- Chen, J., Wu, Z., Augustin-Bauditz, S., Grawe, S., Hartmann, M., Pei, X., Liu, Z., Ji, D. and Wex, H.: Ice-nucleating particle concentrations unaffected by urban air pollution in Beijing, China, *Atmos. Chem. Phys.*, 18(5), 3523–3539, doi:10.5194/acp-18-3523-2018, 2018.
- Chen, Y. and Bond, T. C.: Light absorption by organic carbon from wood combustion, *Atmos. Chem. Phys.*, 10(4), 1773–1787, doi:10.5194/acp-10-1773-2010, 2010.
- Chen, Y., Xie, X., Shi, Z., Li, Y., Gai, X., Wang, J., Li, H., Wu, Y., Zhao, X., Chen, M. and Ge, X.: Brown carbon in atmospheric fine particles in Yangzhou, China: Light absorption properties and source apportionment, *Atmos. Res.*, 244(April), 105028, doi:10.1016/j.atmosres.2020.105028, 2020.
- 585



- Cheng, Y., He, K. B., Zheng, M., Duan, F. K., Du, Z. Y., Ma, Y. L., Tan, J. H., Yang, F. M., Liu, J. M., Zhang, X. L., Weber, R. J., Bergin, M. H. and Russell, A. G.: Mass absorption efficiency of elemental carbon and water-soluble organic carbon in Beijing, China, *Atmos. Chem. Phys.*, 11(22), 11497–11510, doi:10.5194/acp-11-11497-2011, 2011.
- 590 Choudhary, V., Rajput, P. and Gupta, T.: Absorption properties and forcing efficiency of light-absorbing water-soluble organic aerosols: Seasonal and spatial variability, *Environ. Pollut.*, 272, 115932, doi:10.1016/j.envpol.2020.115932, 2021.
- Chowdhury, S., Pozzer, A., Haines, A., Klingmüller, K., Münzel, T., Paasonen, P., Sharma, A., Venkataraman, C. and Lelieveld, J.: Global health burden of ambient PM_{2.5} and the contribution of anthropogenic black carbon and organic aerosols, *Environ. Int.*, 159, 107020, doi:10.1016/j.envint.2021.107020, 2022.
- 595 Collaud Coen, M., Weingartner, E., Apituley, A., Ceburnis, D., Fierz-Schmidhauser, R., Flentje, H., Henzing, J. S., Jennings, S. G., Moerman, M., Petzold, A., Schmid, O. and Baltensperger, U.: Minimizing light absorption measurement artifacts of the Aethalometer: Evaluation of five correction algorithms, *Atmos. Meas. Tech.*, 3(2), 457–474, doi:10.5194/amt-3-457-2010, 2010.
- Cornbleet, P. J. and Gochman, N.: Incorrect least-squares regression coefficients in method-comparison analysis., *Clin. Chem.*, 600 25(3), 432–438, doi:10.1093/clinchem/25.3.432, 1979.
- Corsini, E., Ozgen, S., Papale, A., Galbiati, V., Lonati, G., Fermo, P., Corbella, L., Valli, G., Bernardoni, V., Dell’Acqua, M., Becagli, S., Caruso, D., Vecchi, R., Galli, C. L. and Marinovich, M.: Insights on wood combustion generated proinflammatory ultrafine particles (UFP), *Toxicol. Lett.*, 266, 74–84, doi:10.1016/j.toxlet.2016.12.005, 2017.
- Cross, E. S., Slowik, J. G., Davidovits, P., Allan, J. D., Worsnop, D. R., Jayne, J. T., Lewis, D. K., Canagaratna, M. and 605 Onasch, T. B.: Laboratory and ambient particle density determinations using light scattering in conjunction with aerosol mass spectrometry, *Aerosol Sci. Technol.*, 41(4), 343–359, doi:10.1080/02786820701199736, 2007.
- Cuesta-Mosquera, A., Mocnik, G., Drinovec, L., Müller, T., Pfeifer, S., Minguillon, M. C., Briel, B., Buckley, P., Dudoitis, V., Fernández-García, J., Fernandez-Amado, M., De Brito, J. F., Riffault, V., Flentje, H., Heffernan, E., Kalivitis, N., Kalogridis, A. C., Keernik, H., Marmureanu, L., Luoma, K., Marinoni, A., Pikridas, M., Schauer, G., Serfozo, N., Servomaa, 610 H., Titos, G., Yus-Diez, J., Zioła, N. and Wiedensohler, A.: Intercomparison and characterization of 23 Aethalometers under laboratory and ambient air conditions: Procedures and unit-to-unit variabilities, *Atmos. Meas. Tech.*, 14(4), 3195–3216, doi:10.5194/amt-14-3195-2021, 2021.
- Deming, W. E.: *Statistical Adjustment of Data*, J. Wiley & Sons, Incorporated. [online] Available from: <https://books.google.de/books?id=9awgAAAAMAAJ>, 1943.
- 615 Drinovec, L., Močnik, G., Zotter, P., Prévôt, A. S. H., Ruckstuhl, C., Coz, E., Rupakheti, M., Sciare, J., Müller, T., Wiedensohler, A. and Hansen, A. D. A.: The “dual-spot” Aethalometer: An improved measurement of aerosol black carbon with real-time loading compensation, *Atmos. Meas. Tech.*, 8(5), 1965–1979, doi:10.5194/amt-8-1965-2015, 2015.
- Drinovec, L., Jagodič, U., Pirker, L., Škarabot, M., Kurtjak, M., Vidović, K., Ferrero, L., Visser, B., Röhrbein, J., Weingartner, E., Kalbermatter, D. M., Vasilatou, K., Bühlmann, T., Pascale, C., Müller, T., Wiedensohler, A. and Močnik, G.: A dual-wavelength photothermal aerosol absorption monitor: design, calibration and performance, *Atmos. Meas. Tech.*, 15(12), 3805–
- 620

3825, doi:10.5194/amt-15-3805-2022, 2022.

European Environmental Agency: Air quality in Europe - 2020 report. [online] Available from: <https://www.eea.europa.eu/publications/air-quality-in-europe-2020-report>, 2020.

625 Feng, Y., Ramanathan, V. and Kotamarthi, V. R.: Brown carbon: A significant atmospheric absorber of solar radiation, *Atmos. Chem. Phys.*, 13(17), 8607–8621, doi:10.5194/acp-13-8607-2013, 2013.

Fine, P. M., Cass, G. R. and Simoneit, B. R. T.: Chemical characterization of fine particle emissions from fireplace combustion of woods grown in the northeastern United States, *Environ. Sci. Technol.*, 35(13), 2665–2675, doi:10.1021/es001466k, 2001.

Geng, F., Hua, J., Mu, Z., Peng, L., Xu, X., Chen, R. and Kan, H.: Differentiating the associations of black carbon and fine particle with daily mortality in a Chinese city, *Environ. Res.*, 120, 27–32, doi:10.1016/j.envres.2012.08.007, 2013.

630 Glojek, K., Gregorič, A., Močnik, G., Cuesta-Mosquera, A., Wiedensohler, A., Drinovec, L. and Ogrin, M.: Hidden black carbon air pollution in hilly rural areas—a case study of Dinaric depression, *Eur. J. Geogr.*, 11(2), 105–122, doi:10.48088/ejg.k.glo.11.2.105.122, 2020.

635 Glojek, K., Močnik, G., Alas, H. D. C., Cuesta-Mosquera, A., Drinovec, L., Gregorič, A., Ogrin, M., Weinhold, K., Ježek, I., Müller, T., Rigler, M., Remškar, M., Van Pinxteren, D., Herrmann, H., Ristorini, M., Merkel, M., Markelj, M. and Wiedensohler, A.: The impact of temperature inversions on black carbon and particle mass concentrations in a mountainous area, *Atmos. Chem. Phys.*, 22(8), 5577–5601, doi:10.5194/acp-22-5577-2022, 2022.

Harrison, R. M., Beddows, D. C. S., Jones, A. M., Calvo, A., Alves, C. and Pio, C.: An evaluation of some issues regarding the use of aethalometers to measure woodsmoke concentrations, *Atmos. Environ.*, 80, 540–548, doi:10.1016/j.atmosenv.2013.08.026, 2013.

640 Hartmann, D. L.: Chapter 1 - Introduction to the Climate System, edited by D. L. B. T.-G. P. C. (Second E. Hartmann, pp. 1–23, Elsevier, Boston., 2016.

He, Q., Li, C., Siemens, K., Morales, A. C., Hettiyadura, A. P. S., Laskin, A. and Rudich, Y.: Optical Properties of Secondary Organic Aerosol Produced by Photooxidation of Naphthalene under NO_x Condition, *Environ. Sci. Technol.*, 56(8), 4816–4827, doi:10.1021/acs.est.1c07328, 2022.

645 Herich, H., Gianini, M. F. D., Piot, C., Močnik, G., Jaffrezo, J. L., Besombes, J. L., Prévôt, A. S. H. and Hueglin, C.: Overview of the impact of wood burning emissions on carbonaceous aerosols and PM in large parts of the alpine region, *Atmos. Environ.*, 89, 64–75, doi:10.1016/j.atmosenv.2014.02.008, 2014.

650 Hoffer, A., Gelencsér, A., Guyon, P., Kiss, G., Schmid, O., Frank, G. P., Artaxo, P. and Andreae, M. O.: Optical properties of humic-like substances (HULIS) in biomass-burning aerosols, *Atmos. Chem. Phys.*, 6(11), 3563–3570, doi:10.5194/acp-6-3563-2006, 2006.

Janssen, N. A. H., Hoek, G., Simic-Lawson, M., Fischer, P., van Bree, L., Brink, H. Ten, Keuken, M., Atkinson, R. W., Ross Anderson, H., Brunekreef, B. and Cassee, F. R.: Black carbon as an additional indicator of the adverse health effects of airborne particles compared with pm₁₀ and pm_{2.5}, *Environ. Health Perspect.*, 119(12), 1691–1699, doi:10.1289/ehp.1003369, 2011.

Kalbermatter, D. M., Močnik, G., Drinovec, L., Visser, B., Röhrbein, J., Oscity, M., Weingartner, E., Hyvärinen, A. P. and



- 655 Vasilatou, K.: Comparing black-carbon-and aerosol-absorption-measuring instruments-A new system using lab-generated soot coated with controlled amounts of secondary organic matter, *Atmos. Meas. Tech.*, 15(2), 561–572, doi:10.5194/amt-15-561-2022, 2022.
- Kaskaoutis, D. G., Grivas, G., Oikonomou, K., Tavernaraki, P., Papoutsidaki, K., Tsagkaraki, M., Stavroulas, I., Zarmas, P., Paraskevopoulou, D., Bougiatioti, A., Liakakou, E., Gavrouzou, M., Dumka, U. C., Hatzianastassiou, N., Sciare, J., Gerasopoulos, E. and Mihalopoulos, N.: Impacts of severe residential wood burning on atmospheric processing, water-soluble organic aerosol and light absorption, in an inland city of Southeastern Europe, *Atmos. Environ.*, 280(April), 119139, doi:10.1016/j.atmosenv.2022.119139, 2022.
- 660 Kim, H., Kim, J. Y., Jin, H. C., Lee, J. Y. and Lee, S. P.: Seasonal variations in the light-absorbing properties of water-soluble and insoluble organic aerosols in Seoul, Korea, *Atmos. Environ.*, 129, 234–242, doi:10.1016/j.atmosenv.2016.01.042, 2016.
- 665 Kim, J., Bauer, H., Dobovičnik, T., Hitzenberger, R., Lottin, D., Ferry, D. and Petzold, A.: Assessing optical properties and refractive index of combustion aerosol particles through combined experimental and modeling studies, *Aerosol Sci. Technol.*, 49(5), 340–350, doi:10.1080/02786826.2015.1020996, 2015.
- Koch, D., Bauer, S. E., Del Genio, A., Faluvegi, G., McConnell, J. R., Menon, S., Miller, R. L., Rind, D., Ruedy, R., Schmidt, G. A. and Shindell, D.: Coupled aerosol-chemistry-climate twentieth-century transient model investigation: Trends in short-lived species and climate responses, *J. Clim.*, 24(11), 2693–2714, doi:10.1175/2011JCLI3582.1, 2011.
- 670 Kodros, J. K., Scott, C. E., Farina, S. C., Lee, Y. H., L’Orange, C., Volckens, J. and Pierce, J. R.: Uncertainties in global aerosols and climate effects due to biofuel emissions, *Atmos. Chem. Phys.*, 15(15), 8577–8596, doi:10.5194/acp-15-8577-2015, 2015.
- Kumar, N. K., Corbin, J. C., Bruns, E. A., Massabó, D., Slowik, J. G., Drinovec, L., Močnik, G., Prati, P., Vlachou, A., Baltensperger, U., Gysel, M., El-Haddad, I. and Prévôt, A. S. H.: Production of particulate brown carbon during atmospheric aging of residential wood-burning emissions, *Atmos. Chem. Phys.*, 18(24), 17843–17861, doi:10.5194/acp-18-17843-2018, 2018.
- Lack, D. A. and Langridge, J. M.: On the attribution of black and brown carbon light absorption using the Ångström exponent, *Atmos. Chem. Phys.*, 13(20), 10535–10543, doi:10.5194/acp-13-10535-2013, 2013.
- 680 Lack, D. A., Langridge, J. M., Bahreini, R., Cappa, C. D., Middlebrook, A. M. and Schwarz, J. P.: Brown carbon and internal mixing in biomass burning particles, *Proc. Natl. Acad. Sci. U. S. A.*, 109(37), 14802–14807, doi:10.1073/pnas.1206575109, 2012.
- Laskin, A., Laskin, J. and Nizkorodov, S. A.: Chemistry of Atmospheric Brown Carbon, *Chem. Rev.*, 115(10), 4335–4382, doi:10.1021/cr5006167, 2015.
- 685 Li, C., Hu, Y., Chen, J., Ma, Z., Ye, X., Yang, X., Wang, L., Wang, X. and Mellouki, A.: Physiochemical properties of carbonaceous aerosol from agricultural residue burning: Density, volatility, and hygroscopicity, *Atmos. Environ.*, 140, 94–105, doi:10.1016/j.atmosenv.2016.05.052, 2016.
- Liakakou, E., Kaskaoutis, D. G., Grivas, G., Stavroulas, I., Tsagkaraki, M., Paraskevopoulou, D., Bougiatioti, A., Dumka, U.



- C., Gerasopoulos, E. and Mihalopoulos, N.: Long-term brown carbon spectral characteristics in a Mediterranean city (Athens),
690 *Sci. Total Environ.*, 708, 135019, doi:10.1016/j.scitotenv.2019.135019, 2020.
- Liang, L., Engling, G., Liu, C., Xu, W., Liu, X., Cheng, Y., Du, Z., Zhang, G., Sun, J. and Zhang, X.: Measurement report:
Chemical characteristics of PM_{2.5} during typical biomass burning season at an agricultural site of the North China Plain,
Atmos. Chem. Phys., 21(4), 3181–3192, doi:10.5194/acp-21-3181-2021, 2021.
- Liu, J., Lin, P., Laskin, A., Laskin, J., Kathmann, S. M., Wise, M., Caylor, R., Imholt, F., Selimovic, V. and Shilling, J. E.:
695 Optical properties and aging of light-absorbing secondary organic aerosol, *Atmos. Chem. Phys.*, 16(19), 12815–12827,
doi:10.5194/acp-16-12815-2016, 2016.
- Massabò, D., Caponi, L., Bernardoni, V., Bove, M. C., Brotto, P., Calzolari, G., Cassola, F., Chiari, M., Fedi, M. E., Fermo, P.,
Giannoni, M., Lucarelli, F., Nava, S., Piazzalunga, A., Valli, G., Vecchi, R. and Prati, P.: Multi-wavelength optical
determination of black and brown carbon in atmospheric aerosols, *Atmos. Environ.*, 108, 1–12,
700 doi:10.1016/j.atmosenv.2015.02.058, 2015.
- Mauderly, J. L. and Chow, J. C.: Health Effects of Organic Aerosols, *Inhal. Toxicol.*, 20(3), 257–288,
doi:10.1080/08958370701866008, 2008.
- Mbengue, S., Zikova, N., Schwarz, J., Vodička, P., Šmejkalová, A. H. and Holoubek, I.: Mass absorption cross-section and
absorption enhancement from long term black and elemental carbon measurements: A rural background station in Central
705 Europe, *Sci. Total Environ.*, 794, doi:10.1016/j.scitotenv.2021.148365, 2021.
- Olson, M. R., Garcia, M. V., Robinson, M. A., Rooy, P. Van, Dietenberger, M. A., Bergin, M. and Schauer, J. J.: Journal of
Geophysical Research: Atmospheres fuel combustion source emissions, *J. Geophys. Res. Atmos.*, 6682–6697,
doi:10.1002/2014JD022970. Received, 2015.
- Ozgen, S., Becagli, S., Bernardoni, V., Caserini, S., Caruso, D., Corbella, L., Dell’Acqua, M., Fermo, P., Gonzalez, R., Lonati,
710 G., Signorini, S., Tardivo, R., Tosi, E., Valli, G., Vecchi, R. and Marinovich, M.: Analysis of the chemical composition of
ultrafine particles from two domestic solid biomass fired room heaters under simulated real-world use, *Atmos. Environ.*, 150,
87–97, doi:10.1016/j.atmosenv.2016.11.048, 2017.
- Petzold, A., Ogren, J. A., Fiebig, M., Laj, P., Li, S. M., Baltensperger, U., Holzer-Popp, T., Kinne, S., Pappalardo, G.,
Sugimoto, N., Wehrli, C., Wiedensohler, A. and Zhang, X. Y.: Recommendations for reporting black carbon measurements,
715 *Atmos. Chem. Phys.*, 13(16), 8365–8379, doi:10.5194/acp-13-8365-2013, 2013.
- Pfeifer, S., Birmili, W., Schladitz, A., Müller, T., Nowak, A. and Wiedensohler, A.: A fast and easy-to-implement inversion
algorithm for mobility particle size spectrometers considering particle number size distribution information outside of the
detection range, *Atmos. Meas. Tech.*, 7(1), 95–105, doi:10.5194/amt-7-95-2014, 2014.
- POCITYF: Ioannina - POCITYF Project, [online] Available from: <https://pocityf.eu/city/ioannina/>, 2023.
- 720 Qin, Y. M., Bo Tan, H., Li, Y. J., Jie Li, Z., Schurman, M. I., Liu, L., Wu, C. and Chan, C. K.: Chemical characteristics of
brown carbon in atmospheric particles at a suburban site near Guangzhou, China, *Atmos. Chem. Phys.*, 18(22), 16409–16418,
doi:10.5194/acp-18-16409-2018, 2018.



- R Core Team: R: A language and environment for statistical computing, [online] Available from: <https://www.r-project.org/>, 2020.
- 725 Rissler, J., Nordin, E. Z., Eriksson, A. C., Nilsson, P. T., Frosch, M., Sporre, M. K., Wierzbicka, A., Svenningsson, B., Löndahl, J., Messing, M. E., Sjogren, S., Hemmingsen, J. G., Loft, S., Pagels, J. H. and Swietlicki, E.: Effective density and mixing state of aerosol particles in a near-traffic urban environment, *Environ. Sci. Technol.*, 48(11), 6300–6308, doi:10.1021/es5000353, 2014.
- Sagan, C. and Pollack, J. B.: Anisotropic nonconservative scattering and the clouds of Venus, *J. Geophys. Res.*, 72(2), 469–
730 477, doi:<https://doi.org/10.1029/JZ072i002p00469>, 1967.
- Setyan, A., Zhang, Q., Merkel, M., Knighton, W. B., Sun, Y., Song, C., Shilling, J. E., Onasch, T. B., Herndon, S. C., Worsnop, D. R., Fast, J. D., Zaveri, R. A., Berg, L. K., Wiedensohler, A., Flowers, B. A., Dubey, M. K. and Subramanian, R.: Characterization of submicron particles influenced by mixed biogenic and anthropogenic emissions using high-resolution aerosol mass spectrometry: Results from CARES, *Atmos. Chem. Phys.*, 12(17), 8131–8156, doi:10.5194/acp-12-8131-2012,
735 2012.
- Shamjad, P. M., Tripathi, S. N., Thamban, N. M. and Vreeland, H.: Refractive index and absorption attribution of highly absorbing brown carbon aerosols from an urban Indian city-Kanpur, *Sci. Rep.*, 6(October), 1–7, doi:10.1038/srep37735, 2016.
- Srinivas, B. and Sarin, M. M.: Brown carbon in atmospheric outflow from the Indo-Gangetic Plain: Mass absorption efficiency and temporal variability, *Atmos. Environ.*, 89, 835–843, doi:10.1016/j.atmosenv.2014.03.030, 2014.
- 740 Szopa, S., Naik, V., Adhikary, B., Artaxo, P., Berntsen, T., Collins, W. D., Fuzzi, S., Gallardo, L., Kiendler Scharr, A., Klimont, Z., Liao, H., Unger, N. and Zanis, P.: Short-Lived Climate Forcers. In *Climate Change 2021: The Physical Science Basis. Contribution of Working Group I to the Sixth Assessment Report of the Intergovernmental Panel on Climate Change.*, 2021.
- Therneau, T.: deming: Deming, Theil-Sen, Passing-Bablok and Total Least Squares Regression, [online] Available from:
745 <https://cran.r-project.org/web/packages/deming/index.html>, 2018.
- Turpin, B. J. and Lim, H. J.: Species contributions to pm_{2.5} mass concentrations: Revisiting common assumptions for estimating organic mass, *Aerosol Sci. Technol.*, 35(1), 602–610, doi:10.1080/02786820119445, 2001.
- UNECE: Wood energy on the rise in Europe, [online] Available from: <https://unece.org/climate-change/press/wood-energy-rise-europe#:~:text=Countries in the European Union,increased demand by individual households.> (Accessed 10 November
750 2022), 2022.
- Utry, N., Ajtai, T., Filep, Á., Pintér, M., Török, Z., Bozóki, Z. and Szabó, G.: Correlations between absorption Angström exponent (AAE) of wintertime ambient urban aerosol and its physical and chemical properties, *Atmos. Environ.*, 91, 52–59, doi:10.1016/j.atmosenv.2014.03.047, 2014.
- Vicente, E. D. and Alves, C. A.: An overview of particulate emissions from residential biomass combustion, *Atmos. Res.*,
755 199(March 2017), 159–185, doi:10.1016/j.atmosres.2017.08.027, 2018.
- Wallace, J. M. and Hobbs, P. V.: 3 - Atmospheric Thermodynamics, edited by J. M. Wallace and P. V. B. T.-A. S. (Second E.



- Hobbs, pp. 63–111, Academic Press, San Diego., 2006.
- 760 Wang, J., Nie, W., Cheng, Y., Shen, Y., Chi, X., Wang, J., Huang, X., Xie, Y., Sun, P., Xu, Z., Qi, X., Su, H. and Ding, A.:
Light absorption of brown carbon in eastern China based on 3-year multi-wavelength aerosol optical property observations
and an improved absorption Ångström exponent segregation method, *Atmos. Chem. Phys.*, 18(12), 9061–9074,
doi:10.5194/acp-18-9061-2018, 2018.
- WHO, Janssen, N. A., Gerlofs-Nijland, M. E., Lanki, T., Salonen, R. O., Cassee, F., Hoek, G., Fischer, P., Brunekreef, B. and
Krzyzanowski, M.: Health effects of black carbon, World Health Organization, Regional Office for Europe., 2012.
- 765 Wiedensohler, A., Birmili, W., Nowak, A., Sonntag, A., Weinhold, K., Merkel, M., Wehner, B., Tuch, T., Pfeifer, S., Fiebig,
M., Fjåraa, A. M., Asmi, E., Sellegri, K., Depuy, R., Venzac, H., Villani, P., Laj, P., Aalto, P., Ogren, J. A., Swietlicki, E.,
Williams, P., Roldin, P., Quincey, P., Hüglin, C., Fierz-Schmidhauser, R., Gysel, M., Weingartner, E., Riccobono, F., Santos,
S., Gröning, C., Faloon, K., Beddows, D., Harrison, R., Monahan, C., Jennings, S. G., O’Dowd, C. D., Marinoni, A., Horn, H.
G., Keck, L., Jiang, J., Scheckman, J., McMurry, P. H., Deng, Z., Zhao, C. S., Moerman, M., Henzing, B., De Leeuw, G.,
Löschau, G. and Bastian, S.: Mobility particle size spectrometers: Harmonization of technical standards and data structure to
770 facilitate high quality long-term observations of atmospheric particle number size distributions, *Atmos. Meas. Tech.*, 5(3),
657–685, doi:10.5194/amt-5-657-2012, 2012.
- Xu, H., Ren, Y., Zhang, W., Meng, W., Yun, X., Yu, X., Li, J., Zhang, Y., Shen, G., Ma, J., Li, B., Cheng, H., Wang, X., Wan,
Y. and Tao, S.: Updated global black carbon emissions from 1960 to 2017: Improvements, trends, and drivers, *Environ. Sci.*
Technol., 55(12), 7869–7879, doi:10.1021/acs.est.1c03117, 2021.
- 775 Yus-Díez, J., Bernardoni, V., Močnik, G., Alastuey, A., Ciniglia, D., Ivančič, M., Querol, X., Perez, N., Reche, C., Rigler, M.,
Vecchi, R., Valentini, S. and Pandolfi, M.: Determination of the multiple-scattering correction factor and its cross-sensitivity
to scattering and wavelength dependence for different AE33 Aethalometer filter tapes: A multi-instrumental approach, *Atmos.*
Meas. Tech. Discuss., 29, 1–30, doi:10.5194/amt-2021-46, 2021.
- 780 Zanatta, M., Gysel, M., Bukowiecki, N., Müller, T., Weingartner, E., Areskou, H., Fiebig, M., Yttri, K. E., Mihalopoulos, N.,
Kouvarakis, G., Beddows, D., Harrison, R. M., Cavalli, F., Putaud, J. P., Spindler, G., Wiedensohler, A., Alastuey, A.,
Pandolfi, M., Sellegri, K., Swietlicki, E., Jaffrezo, J. L., Baltensperger, U. and Laj, P.: A European aerosol phenomenology-5:
Climatology of black carbon optical properties at 9 regional background sites across Europe, *Atmos. Environ.*, 145, 346–364,
doi:10.1016/j.atmosenv.2016.09.035, 2016.
- 785 Zhang, W., Wang, W., Li, J., Ma, S., Lian, C., Li, K., Shi, B., Liu, M., Li, Y., Wang, Q. Q., Sun, Y., Tong, S. and Ge, M.:
Light absorption properties and potential sources of brown carbon in Fenwei Plain during winter 2018–2019, *J. Environ. Sci.*
(China), 102, 53–63, doi:10.1016/j.jes.2020.09.007, 2021.
- Zhang, X., Kim, H., Parworth, C. L., Young, D. E., Zhang, Q., Metcalf, A. R. and Cappa, C. D.: Optical Properties of
Wintertime Aerosols from Residential Wood Burning in Fresno, CA: Results from DISCOVER-AQ 2013, *Environ. Sci.*
Technol., 50(4), 1681–1690, doi:10.1021/acs.est.5b04134, 2016.
- 790 Zhang, Y., Albinet, A., Petit, J. E., Jacob, V., Chevrier, F., Gille, G., Pontet, S., Chrétien, E., Dominik-Sègue, M., Levigoureux,



G., Močnik, G., Gros, V., Jaffrezo, J. L. and Favez, O.: Substantial brown carbon emissions from wintertime residential wood burning over France, *Sci. Total Environ.*, 743, doi:10.1016/j.scitotenv.2020.140752, 2020.

Zhu, C. S., Cao, J. J., Huang, R. J., Shen, Z. X., Wang, Q. Y. and Zhang, N. N.: Light absorption properties of brown carbon over the southeastern Tibetan Plateau, *Sci. Total Environ.*, 625, 246–251, doi:10.1016/j.scitotenv.2017.12.183, 2018.